UNIVERSITÀ DEGLI STUDI DI PADOVA

Dipartimento di Fisica e Astronomia “Galileo Galilei”

Master Degree in Physics

Final Dessertation

Study of tunneling effect in Nuclear Physics through the measurement of heavy ion fusion; consequences for astrophysics

Thesis supervisor

Prof. Giovanna Montagnoli

Thesis co-supervisor

Dr. Alberto M. Stefanini

Candidate

Omorjit Singh Khwairakpam

Academic Year 2018/19

Abstract

The present thesis reports on the recent measurement of the fusion excitation function for the system ^{12}C+^{24}Mg (Q_{fus}= +16.3 MeV) down to around 10 μb, in order to investigate whether fusion hindrance shows up, phenomenologically marked by the observation of a maximum of the S-factor vs. energy. The aim was to search evidence for fusion hindrance in medium-light systems with positive Q-values, besides the heavier cases where hindrance is recognized to be a general phenomenon. The system ^{12}C+^{24}Mg is very close to the ^{16}O+^{16}O and ^{12}C+^{12}C systems that are important for the late evolution of heavy stars. The experiment has been performed in inverse kinematics using the ^{24}Mg beam from the XTU Tandem accelerator of Labaratori Nazionali di Legnaro (LNL) in the energy range 26-52 MeV with an intensity of 4-8 pnA. The targets were ^{12}C evaporations 50 μg/cm^2 thick, isotopically enriched to 99.9%. The fusion-evaporation residues were detected at small angles in a TOF-ΔE-E telescope following the electrostatic beam deflector in use at LNL.

Previous measurements of fusion cross section for ^{12}C+^{24}Mg were limited to above-barrier energies. The new results show that the S-factor develops a clear maximum vs. energy, indicating the presence of hindrance in this system below the Coulomb barrier energy.

The hindrance threshold in this system follows rather closely a systematics obtained for several medium-light systems together with a phenomenological estimate that fits well also the new data point for this case. The calculated fusion cross section at threshold is very large (σ_s=1.6mb) and it is indeed the largest found for medium-light systems.

This has allowed to identify the hindrance phenomenon in a favorable condition. It may even be possible to extend the measurements further down in energy to better establish the position of the S-factor maximum. The experimental data have been compared with the results of coupled channel calculations including the lowest quadrupole vibrations of ^{24}Mg. With this comparison, the hindrance behaviour has been better evidenced at deep sub-barrier energies.

Acknowledgement

I would like to express my deepest appreciation to my thesis supervisor, Giovanna Montagnoli, and co-supervisor, Alberto M. Stefanini, for the continuous support throughout my master thesis and for their patience, motivation, enthusiasm and immense knowledge. Their guidance helped me a lot in carrying out the research work and writing of this thesis. I could not have imagined better advisors for my master thesis.

I would like to extend my gratitude to Dr. Giulia Colucci for her support and guidance during the thesis work.

I also thank Dr. Fabiana Gramegna and Dr. Magda Cicerchia for extending their helping hands in times of need.

My sincere thanks goes to Crista Buoso for making it easier in adapting to a scientific research community and for her emotional support and wise advises.

I am also thankful to the professors and researchers involved in the NucPhys programme for having motivated me. My special thanks goes to Prof. Jose M. Arias who has always supported me from the beginning of the programme.

Last but not the least, I would like to thank my family and friends for believing in me and being there for me outside work and research.

Contents

List of Figures

List of Tables

Chapter 1

Introduction

The fusion of heavy ions has captured the interest of many nuclear physicists over the last few decades. The interest in this research area goes back to the quest of extending the periodic table beyond the elements that can be synthesized using neutrons, light charged particles and heavy actinide targets. Availability of new experimental techniques and methods has motivated to dig deeper into the area of research.

Heavy ion fusion concerns with the study of collision of two heavy ions to form a compound nucleus. Classically, in order to form a compound nucleus, the ions should collide with an energy greater than the Coulomb barrier. Coulomb barrier of a system of colliding nuclei arises from the balance between the repulsive Coulomb term and the attractive nuclear term of the potential. For energies below the Coulomb barrier, it is classically forbidden to form a compound nucleus. However, even at energies below the Coulomb barrier, compound nuclei are formed. The explanation lies in the quantum tunneling effect.

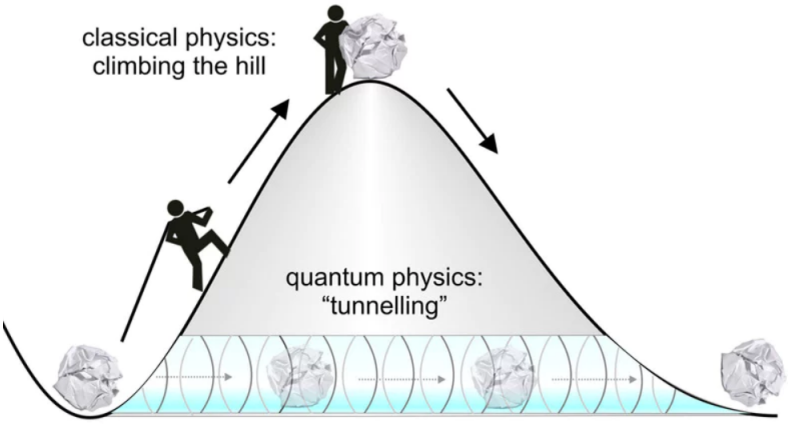

Figure 1.1: A simplified demonstration of quantum tunneling compared to Classical Physics (Credit: Max Planck Institute for Quantum Optics)

In quantum tunneling effect, there is always a probability that the system will appear on the other side of the barrier, even though the energy of the system is lower than the barrier. A simplified demonstration of this effect is shown in Fig. 1.1. In the sub-barrier fusion of heavy ions, quantum tunneling plays a very important role.

Heavy-ion fusion is a complex phenomenon whose study involves several experiments and theoretical efforts. The limits to this research field have been further pushed with the development of new methods and availability of medium-mass heavy ion beams. Large Tandem electrostatic accelerators have contributed significantly in the advancement of the research area by making it possible to produce heavy-ion beams with sufficient energy to overcome the Coulomb barrier in collisions with targets of almost all elements.

Wong formula [1] based on the quantal penetration of the barrier successfully explained the fusion cross-sections of light heavy-ion systems. However, in the late 70’s, there were strong pushbacks in the experimental and theoretical studies on near- and sub-barrier heavy-ion fusion. For heavier systems, the experimental values were no more consistent with the theoretical calculations of the Wong Formula. Two basic kinds of phenomenon, which were not accounted for before, were evidenced. One was the significant enhancement of fusion cross-sections in the sub-barrier region and the other was the strong isotopic effect in the fusion

cross-sections. This indicated the existing connection between the sub-barrier fusion dynamics and the low-lying collective structures of the two colliding nuclei [2, 3]. Therefore, the effect of the couplings between the relative motion and the nuclear intrinsic degree of freedom need to be considered.

To take this into account, the coupled-channels (CC) model [3] was developed. It involves a large number of channels and so several approximations were adopted to reduce the number of channels. Some of the approximations are- 'Incoming Wave Boundary Conditions', 'Sudden limit approximation', 'Constant coupling approximation' and 'Iso-centrifugal approximation'. The CC model was quite successful in explaining the enhancement of the fusion cross-sections in the sub-barrier energies. The discovery of enhancement of sub-barrier fusion started a new generation of experiments.

In the early 2000's, an experiment to measure the fusion cross-sections of ^{60}Ni+ ^{89}Y [4] was performed at Argonne National Lab. The results showed an unexpected behaviour at extreme sub-barrier energies. The fusion cross-sections drop much faster than predicted by standard CC calculation. This was referred to as the 'hindrance' effect. It has since been confirmed in fusion measurements of many other light and medium-heavy systems, although the origin of this effect is still unclear. Several experiments have been performed in different labs to observe and explain this effect in the deep sub-barrier region.

It is of paramount importance to study this existing competition between the opposite trend originated from near-barrier enhancements and hindrance at lower energies. Availability of good quality heavy radioactive beams with high intensity will certainly help in studying these effects more deeply.

One of the most important application of the 'hindrance' effect lies with the light heavy-ion systems of astrophysical importance. If the phenomenon exists in light systems, the fusion cross-sections near the Gamow peak would be substantially smaller than expected previously by simple extrapolation of the high-energy trends [5]. Several studies have been performed on systems such as ^{12}C+^{12}C, ^{12}C+^{16}O and ^{16}O+^{16}O, and also the near-by systems of slightly heavier masses. One such example of slightly heavier system is the case of ^{12}C+^{30}Si where the 'hindrance' effect has been observed [6]. The aim of studying these slightly heav-

ier systems is to provide the guideline to extrapolate the behaviour to lighter systems of astrophysical importance.

In the current thesis work, the $^{12}C+^{24}Mg$ system has been studied. Fusion cross-sections have been measured above and below the Coulomb barrier. The results have been compared with the standard CCFULL calculations [7] to observe the existence of hindrance effect in deep sub-barrier energies.

Chapter 2

Sub-barrier fusion

2.1 One-dimensional model

2.1.1 Ion-ion potential and the Coulomb barrier

The one-dimensional potential model is the simplest approach to the heavy ion fusion reactions. In this model, the projectile and the target nuclei are treated as being without internal structure. Since the internal structures are not considered, the potential of the system is a function of only the relative distance r between the projectile and the target.

In heavy-ion fusion, the term 'Coulomb barrier' refers to the barrier formed by the repulsive Coulomb interaction and the attractive nuclear interaction in a central (s-wave) collision.

The potential consists of two parts namely, the Coulomb potential $\mathrm{V}_C(r)$ and the nuclear potential $\mathrm{V}_N(r)$.

$$V(r) = V_C(r) + V_N(r) \tag{2.1}$$

The nuclear potential plays a crucial role to establish the Coulomb barrier along with the Coulomb potential. Moreover, it also establishes the couplings to the nuclear excited states of the interacting nuclei. The Woods-Saxon nuclear potential is given by,

$$V_N(r) = -\frac{V_o}{1 + exp(r - R_o)/a_o} \tag{2.2}$$

where R_o is the radius, V_o is the depth and a_o is the diffuseness of the potential. There is a standard set of parameters that is consistently used for the analysis of elastic scattering data [8, 9]. This empirical potential is referred to as Akyuz-Winther potential.

The set of parameters for Akyuz-Winther potential is described below:

$$\begin{aligned} V_o &= 16\pi\gamma a_o \frac{R_p R_t}{R_p + R_t} \\ R_o &= R_p + R_t \\ a_o &= \frac{1}{1.17[1 + 0.53(A_p^{-1/3} + A_t^{-1/3})]} \\ R_i &= (1.2A_i^{1/3} - 0.09)fm; \qquad i = t, p \\ \gamma &= 0.95[1 - 1.8(A_p - 2Z_p)(A_t - 2Z_t)(A_p/A_t)] \end{aligned} \tag{2.3}$$

where R_p, R_t are the radii of the projectile and the target respectively, and A_p, A_t are the mass number of the projectile and the target respectively.

The Akyuz-Winther potential is a smooth function of the mass numbers of the reacting nuclei. Experimental angular distributions of elastic and inelastic scattering for many systems have been successfully reproduced with this nuclear potential. However, recent results have pointed to the fact that the Akyuz-Winther parametrization is unrealistic for overlapping nuclei and provides a poor description of the fusion data at extreme sub-barrier energies. The fusion cross-sections, for some systems, at energies above and below the Coulomb barrier are overestimated if the same potential, that fits elastic and inelastic scattering data is used. The reason is that heavy-ion scattering is a process which involves the surface of the nucleus, while fusion implies a stronger overlap of the interacting nuclei [10]. This problem can be solved by using a double-folding parameter and by adjusting it for overlapping nuclei in order to provide a better description at very low energies. In double folding model, the nucleus-nucleus potential is given by the expression:

$$V(r) = \int dr_1 \int dr_2 \rho_p(r_1)\rho_t(r_2)v_{NN}(r_2 - r_1 - r) \tag{2.4}$$

where ρ_p and ρ_t are the densities of the projectile and the target respectively, and v_{NN} is the effective nucleon-nucleon interaction. The parameters of the potential are chosen in order to reproduce the experimental data on the phase-shifts

of nucleon-nucleon scattering, deuteron bound state properties and some other experimental characteristics.

The Coulomb potential between two point-like charged particles, placed at a distance r, is given by:

$$V_C(r) = \frac{1}{4\pi\epsilon_o}\frac{Z_p Z_t}{r}e^2 \tag{2.5}$$

where e is the electronic charge and Z_p and Z_t are the projectile and target atomic numbers respectively. The above expression does not take into account the structure of the nuclei and is valid for the region where the projectile and target do not significantly overlap with each other. If r_p and r_t denote the radii of the projectile and the target respectively, Eq. 2.5 is valid only if $r \geq r_p + r_t$.

Alternatively, it can be assumed that the target nucleus is a sphere with a uniform charge Z_t and a radius R, whereas the projectile nucleus is treated as a point-like charge. The Coulomb potential in this case is given by,

$$V(r) = \frac{1}{4\pi\epsilon_o} Z_p Z_t e^2 \begin{cases} \frac{1}{r} & \text{if } r > R_C \\ \frac{1}{2R_C}\left(3 - \frac{r^2}{R^2}\right) & \text{if } r < R_C \end{cases} \tag{2.6}$$

where R_C is the Coulomb radius and is given by $R_C = 1.44(A_p^{1/3} + A_t^{1/3})$ fm.

In heavy ion reactions, the Coulomb potential plays a very important role due to its dependence on the atomic numbers.

Fig. 2.1 shows the potential V(r) for the s-wave scattering of ^{16}O+^{144}Sm reaction. In order for the fusion reaction to occur, the colliding nuclei must overlap significantly. The distance at which the colliding nuclei start to overlap significantly is called the 'touching radius' R_{touch} and the Coulomb barrier is placed outside this radius. So, in the classical picture, fusion reaction would not occur if the Coulomb barrier cannot be overcome.

In general, there is a 'centrifugal' component to the Coulomb barrier in the case of non-central collisions. The centrifugal barrier also plays an important role in the fusion reaction at high energies. The centrifugal barrier is defined as

$$V_l = \frac{\hbar^2}{2\mu}\frac{l(l+1)}{R_b^2} \tag{2.7}$$

where μ is the reduced mass of the system, R_b is the position of the barrier and l is the associated angular momentum.

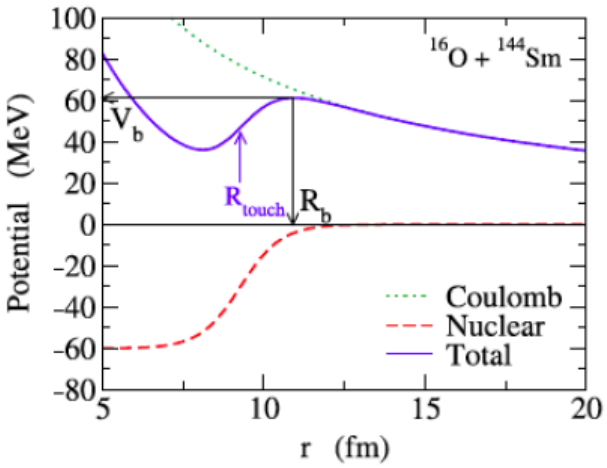

Figure 2.1: Internucleus potential for the ^{16}O+ ^{144}Sm reaction [10]. The green, red and blue lines represent the Coulomb, nuclear and total potential, respectively. The height V_b, position R_b of the Coulomb barrier and the touching radius R_{touch} are indicated.

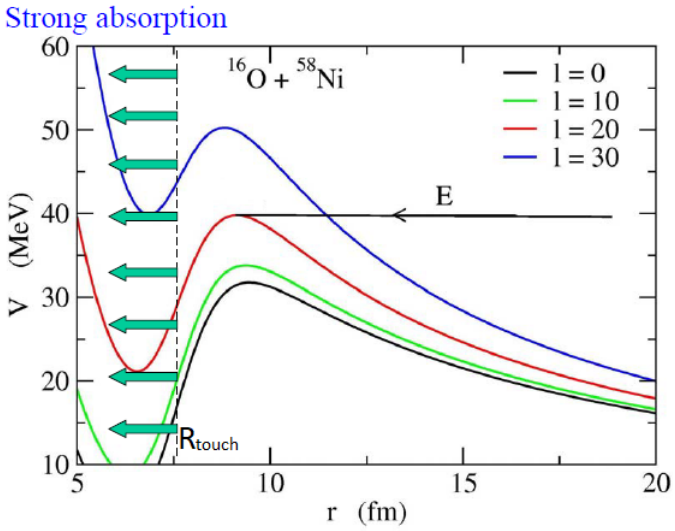

Figure 2.2: Centrifugal barrier of the system ^{16}O+^{58}Ni for different values of angular momentum [11]. The region $r < R_{touch}$ shows strong absorption.

The contribution of the centrifugal barrier increases with higher angular momentum as can be seen in Fig. 2.2. The centrifugal barrier increases the height of the Coulomb barrier while at the same time decreases the depth of the pocket

in the nucleus-nucleus potential.

It can be considered that the capture and subsequent fusion of the system takes place if the system enters the potential pocket. This hypothesis is valid for systems with kinetic energies that are not significantly higher than the Coulomb barrier. At high energies, higher angular momenta may contribute to the fusion process. This decreases the depth of the potential pocket until it disappears above a critical value l_{crit} [12].

$$l_{crit} = R_b \sqrt{\frac{2\mu}{\hbar^2}(E - V_b)} \tag{2.8}$$

where μ is the reduced mass, E is the energy, and V_b is the height and R_b is the position of the barrier. When the value of the angular momentum is lower than l_{crit}, the system is captured inside the pocket and can lead to the formation of a compound nucleus. This is attributed to the fact that for values lower than l_{crit}, dissipative forces reduce the initial angular momentum and consequently the centrifugal potential of the system. If the value is higher than l_{crit}, the process of capture does not take place. However, there is dissipation of energy and exchange of nucleons during the period of contact after which the colliding nuclei separate.

The heavy ion fusion usually leads to the production of a compound nucleus which is at high excitation energy. There are typically two modes of decay that follows: evaporation and fission.

Evaporation refers to the emission of light particles with Z$\leq$ 2 such as neutrons, protons and alpha particles. The nucleus left after this process is referred to as the 'evaporation residue'. In the experiment performed with the system ^{12}C+^{24}Mg, the excitation energy is of the range 25 - 33.5 MeV. In this range of mass and excitation energy, the dominant form of de-excitation of the compound nucleus is evaporation [13].

However, in the fission process which is typical of heavy nuclei, the compound nucleus splits into two fragments of comparable masses. The probability of the fission process is higher for heavier systems compared to lighter systems. There is a strong deformation induced by the repulsive force of the protons and at the same time, there are surface effects which tend to re-establish a spherical shape. The competition between these two effects result in fission of heavy compound

nuclei.

2.1.2 Fusion cross-section

In the one-dimensional potential, the relative motion of the colliding nuclei is the only variable. In the case where the atomic numbers Z of the nuclei are high, a greater overlap of the densities of the colliding nuclei is required to overcome the barrier which is directly proportional to the product of the charges of the colliding nuclei. When there is significant overlap, the nucleon-nucleon interaction becomes dominant and leads to a substantial loss of kinetic energy and angular momentum of the relative motion. As a result, fusion of the two nuclei that cannot escape the potential pocket, takes place.

The transmission co-efficient $T_l(E)$ describes the probability that the system with angular momentum l at energy E will cross the barrier overcoming the total potential. In the one-dimensional model, the interaction is closely linked to the transmission co-efficient. The fusion cross-section of a partial wave with angular momentum l is expressed as,

$$\sigma_l(E) = \pi \lambda\!\!\!^{-2}(2l+1)T_l(E) \tag{2.9}$$

where $\lambda\!\!\!^{-}$ is the reduced de Broglie wavelength of the relative motion.

The total cross-section is obtained by the sum of all the partial waves. However, as discussed before, not all the partial waves take part in the fusion process. Only values of angular momentum up to l_{crit} contribute to the fusion cross-section. Considering that, classically, the probability of the l^{th} partial wave to overcome the Coulomb barrier and lead to fusion is 'one' for $l \leq l_{crit}$ and 'zero' for $l > l_{crit}$, the fusion cross-section can be expressed as,

$$\sigma^{fus}(E) = \sum_{l=0}^{l_{crit}} \pi \lambda\!\!\!^{-2}(2l+1)T_l(E) \tag{2.10}$$

The transmission coefficient can be calculated in different ways. One is to derive from the solution of the Schrödinger equation, Eq.(2.30). Another way is to use the Hill-Wheeler approximation [14], where the Coulomb barrier is approximated by a parabola:

$$V_l(r) \sim V_{bl} - \frac{1}{2}\mu\Omega_l^2(r - R_{bl})^2 \tag{2.11}$$

where V_{bl} is the barrier height, Ω_l is the curvature and R_{bl} is the position of the barrier relative to the l^{th} wave. The corresponding transmission coefficient, within this approximation, is analytically calculated [14] as:

$$T_l(E) = \frac{1}{1 + exp[\frac{2\pi}{\hbar\Omega_l}(V_{bl} - E)]} \tag{2.12}$$

The curvature Ω_l is defined as:

$$\Omega_l = \sqrt{-\frac{1}{\mu}\frac{\delta^2 V_l(r)}{\delta r^2}\bigg|_{r=R_{bl}}} \tag{2.13}$$

The transmission coefficient is replaced in Eq. (2.10). The fusion cross-section can, now, be expressed as:

$$\sigma^{fus}(E) = \sum_{l=0}^{l_{crit}} \pi \lambda\!\!\!^{-2} \frac{(2l+1)}{1 + exp[\frac{2\pi}{\hbar\Omega_l}(V_{bl} - E)]} \tag{2.14}$$

If it is assumed that both the curvature and the position of the Coulomb barrier are independent of the angular momentum l, then a simpler expression, where the values approximate to the ones for s-wave (l=0), is obtained i.e.

$$\begin{aligned} R_{bl} &\sim R_{bo} \\ \Omega_l &\sim \Omega_o \end{aligned} \tag{2.15}$$

The height of the barrier relative to the l^{th} wave can therefore be expressed as:

$$V_{bl} = V_{bo} + \frac{\hbar^2}{2\mu}\frac{l(l+1)}{R_{bo}^2} \tag{2.16}$$

The dependence of the transmission coefficient on the angular momentum can, then, be approximated by shifting the incident energy by a centrifugal term:

$$T_l(E) = T_o\Big(E - \frac{\hbar^2}{2\mu}\frac{l(l+1)}{R_{bo}^2}\Big) \tag{2.17}$$

Considering that many partial waves contribute to the fusion cross-section, Eq. (2.10) can be expressed in the form of integral as:

$$\sigma^{fus}(E) = \pi \lambda\!\!\!^{-2} \int_0^{l_{crit}} (2l+1) T_l(E) dl \tag{2.18}$$

If the variables are changed from l to $l(l+1)$, the integral can be explicitly calculated. This leads to the Wong formula [1]:

$$\sigma^{fus}(E) = \frac{\hbar\Omega_o R_{bo}}{2E} ln\Big(1 + exp\Big[\frac{2\pi}{\hbar\Omega_o}(E - V_{bo})\Big]\Big) \tag{2.19}$$

For energies higher than the Coulomb barrier($E \gg V_{bo}$), the cross-section can be approximated as:

$$\sigma^{fus}(E) = \pi R_{bo}^2\Big(1 - \frac{V_{bo}}{E}\Big) \tag{2.20}$$

Considering Eq. (2.10), for higher energies, and assuming T_l=0 for $l > l_{crit}$ and T_l=1 for $l \leq l_{crit}$, the fusion cross-section can be expressed as:

$$\sigma^{fus}(E) = \sum_{l=o}^{l_{crit}} \pi\lambda\!\!\!^{-2}(2l+1) \simeq \pi\lambda\!\!\!^{-2} l_{crit}^2 \tag{2.21}$$

By replacing the value of l_{crit} from Eq. (2.8) in the above expression, Eq. (2.20) can be obtained.

For energies lower than the Coulomb barrier($E \ll V_{bo}$), the cross-section can be approximated as:

$$\sigma^{fus}(E) = \frac{\hbar\Omega_o R_{bo}}{2E} exp\Big[\frac{2\pi}{\hbar\Omega_o}(E - V_{bo})\Big] \tag{2.22}$$

So for the energies below the Coulomb barrier the cross section depends exponentially on the difference (E - V_{bo}).

2.1.3 Validity of the one-dimensional model

The one-dimensional model has successfully explained the fusion cross section in light systems. Even in the case of heavier systems above the Coulomb barrier, it successfully reproduces the experimental fusion cross-section. However, for heavier systems at sub-barrier energies, the model underestimates the fusion cross-section. This has suggested the need for another model that takes into account other degrees of freedom taking part in the fusion process besides the relative motion of the two nuclei.

The reaction study of the ^{16}O+^{144,148,154}Sm [15] clearly manifested the influence of the nuclear structure on the sub-barrier fusion. In Fig. 2.3 (left), it is

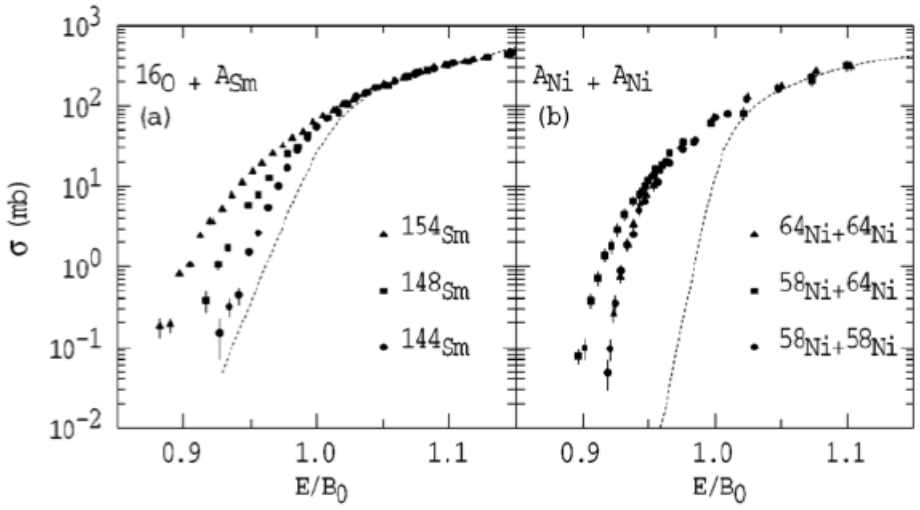

Figure 2.3: On the left, the excitation function of ^{16}O on Sm isotopes [15], where a significant increase of the cross section with increasing mass and isotope deformation is observed. On the right, the excitation functions of ^{58}Ni + ^{58}Ni, ^{58}Ni + ^{64}Ni and ^{64}Ni + ^{64}Ni [16], where the influence of the transfer channels on the fusion process is highlighted. The dashed curves indicate the excitation function in the one-dimensional barrier model [17]

observed that the fusion cross-sections, at higher energies, are in agreement with one another and also with the one-dimensional model calculation. However, at sub-barrier energies, all the excitation functions are strongly enhanced with respect to the one-dimensional model calculation. The fusion cross-section increases with higher deformation of Sm isotopes.

Fig. 2.3 (right), shows the comparison ^{58}Ni+^{58}Ni, ^{58}Ni + ^{64}Ni and ^{64}Ni + ^{64}Ni systems. The three systems also showed the enhancement in the excitation function at sub-barrier energies. Another interesting observation was also made where a more gradual decrease of the excitation function for ^{58}Ni + ^{64}Ni with respect to the other two systems was observed. This trend was associated with the availability of positive Q-value neutron transfer channels for^{58}Ni + ^{64}Ni, which is not the case for the other two systems. This evidence raised the hypothesis that the fusion process may be influenced by specific reaction channels.

Evidences from these results and other subsequent studies attribute the en-

hancement of the fusion cross-sections at sub-barrier energies to:

- the existence of collective excitation modes (surface modes) in the interacting nuclei of vibrational and/or rotational nature
- transfer processes that may take place during the collision

In addition to the low-lying collective excitation, there are several other modes of excitation which may influence the fusion cross-section. Couplings to giant resonances are strong due to their collective character. However, owing to their high excitation energies [18], their effects are taken into account in the choice of the ion-ion potential which is renormalized by those high energy excitations [19]. Also, there are non-collective excitations that couple only to the ground state. These excitations do not significantly affect heavy-ion fusion reactions even if the non-collective states are abundant [20].

Therefore, another model which takes into account the effect of the nuclear structure in the fusion reaction in a more quantitative way is necessary. This is provided by the coupled-channels model.

2.2 Coupled-Channels model

When a collision between two nuclei is considered in the presence of coupling of the relative motion of the interacting nuclei to a nuclear intrinsic motion ζ, the Hamiltonian of the system is,

$$H(r,\zeta) = H_o(\zeta) + T(r) + V(r) + V_c(r,\zeta) \tag{2.23}$$

where $H_o(\zeta)$ is the Hamiltonian describing the internal degrees of freedom, T(r)+V(r) is the one-dimensional Hamiltonian and $V_c(r,\zeta)$ is the coupling term.

Therefore, the stationary Schrodinger equation is

$$\left[-\frac{\hbar^2}{2\mu}\frac{d^2}{dr^2} + \frac{l(l+1)\hbar^2}{2\mu r^2} + V(r) - E\right]\psi(r,\zeta) = -\left[H_o(\zeta) + V_c(r,\zeta)\right]\psi(r,\zeta) \tag{2.24}$$

If $\chi_j(\zeta)$ represent the eigenstates of the intrinsic Hamiltonian $H_o(\zeta)$ and ϵ_j represent the eigenvalue energies, the ensemble of the eigenstates constitutes a complete orthonormal system for the Hilbert space which defines the solution of Eq. (2.24). Under this condition, the function $\psi(r,\zeta)$ can be expanded in terms of $\chi_j(\zeta)$ as follow:

$$\psi(r,\zeta) = \sum_j \phi_j(r)\chi_j(\zeta) \tag{2.25}$$

where $\phi_j(r)$ represents the distorted wave of the relative motion of the j^{th} channel.

A complete orthonormal base of the eigensates $|j>$ of the intrinsic Hamiltonian is considered. According to Dirac formalism, the condition $H_o|j>=\epsilon_j|j>$ can be satisfied if the wave function is expressed as:

$$\psi(r) = \sum_j \phi_j(r)|j> \tag{2.26}$$

Inserting Eq. (2.26) in Eq. (2.24), a set of differential equations is obtained as follows:

$$\sum_j \left[-\frac{\hbar^2}{2\mu}\frac{d^2}{dr^2} + \frac{l_j(l_j+1)\hbar^2}{2\mu r^2} + V(r) - E\right]\phi_j(r)|j> = -\sum_j \left[H_o(\zeta) + V_c(r,\zeta)\right]\phi_j(r)|j> \tag{2.27}$$

The base of the eigenstates $|j>$ is orthonormal as mentioned before. If Eq. (2.27) is multiplied with $<i|$, a new set of coupled equations is obtained as follows:

$$\left[-\frac{\hbar^2}{2\mu}\frac{d^2}{dr^2} + \frac{l_i(l_i+1)\hbar^2}{2\mu r^2} + V(r) - E \right]\phi_i(r) = -\sum_j M_{ij}\phi_j(r) \tag{2.28}$$

where M_{ij} are the coupling matrix elements among the eigenstates related to the internal energy. Solutions to Eq. (2.28) are the wave functions ϕ(r) of the relative motion of the two interacting nuclei.

The coupling matrix elements M_{ij} are given by,

$$M_{ij} = \epsilon_i\delta_{ij} + < i|V_c(r,\zeta)|j > \tag{2.29}$$

which constitute a symmetric matrix.

The coupling matrix M can be factorized to decouple the solutions, if it is a diagonal matrix. Taking this into consideration, some approximations are made in order to decouple the solutions.

2.2.1 Approximations

The coupled-channels model takes into account, for each partial wave l_i, all the coupling orders between channels leading to the same total angular momentum J of the system. Each i^{th} channel denotes an intrinsic state and the model provides a system of differential equations for each value of i. Each equation associated with the partial wave l_i has to be solved.

One of the main problems in solving these equations by numerical means is the large number of channels involved in describing the reaction. It makes the decoupling difficult and the numerical calculations long. Taking this into consideration, several approximations are made to reduce the number of channels and simplify the calculations. The system of differential equations can also be solved using dedicated programs such as CCFULL [7].

Incoming Wave Boundary Conditions

In the potential model, an imaginary part $W(r)$ which simulates the absorption in the fusion reaction channel is included in the internuclear potential $V(r)$. So the Schrodinger equation takes the form

$$\left[-\frac{\hbar^2}{2\mu}\frac{d^2}{dr^2} + \frac{l(l+1)\hbar^2}{2\mu r^2} + V(r) - iW(r) - E \right] u_l(r) = 0 \tag{2.30}$$

where $u_l(r)$, according to typical scattering process boundary conditions, is given by

$$\begin{aligned} u_l(r) &\sim r^{l+1} && r \to 0 \\ u_l(r) &\simeq H_l^{(-)}(kr) - S_l H_l^{(+)}(kr) && r \to \infty \end{aligned} \tag{2.31}$$

where $H_l^{(+)}$ and $H_l^{(-)}$ are the outgoing and the incoming Coulomb wave functions and S_l is the nuclear matrix.

The associated wave number with the energy E is

$$k = \sqrt{2\mu E/\hbar^2} \tag{2.32}$$

The total absorption cross-section can be considered as the fusion cross-section, if the imaginary part $W(r)$ is well confined inside the Coulomb barrier [10].

$$\sigma_{fus}(E) \sim \sigma_{abs}(E) = \frac{\pi}{k^2}\sum_l 2l(l+1)(1-|S_l|^2) \tag{2.33}$$

In heavy ion fusion reactions, it is more convenient to apply the 'incoming wave boundary condition'(IWBC) instead of using the regular boundary condition at the origin as expressed by Eq. (2.31) where an imaginary part $W(r)$ is introduced [2]. In the case of IWBC, it is assumed that there is strong absorption within the inner region of the potential and so the incoming flux never returns back. The wave function, under this condition, is given by

$$u_l(r) = \sqrt{\frac{k}{k_l(r)}} T_l exp\left[-i\int_r^{r_{abs}} k_l(r')dr' \right] \qquad r \le r_{abs} \tag{2.34}$$

where T_l is the transmission coefficient and r_{abs} is the absorption radius, which is assumed to be inside the Coulomb barrier. The radius r_{abs} corresponds, conventionally, to the minimum of the interaction potential [7].

For the l^{th} partial wave, the local wave number of the energy is given by

$$k_l(r) = \sqrt{\frac{2\mu}{\hbar^2}\left[E - V(r) - \frac{l(l+1)\hbar^2}{2\mu r^2}\right]} \tag{2.35}$$

The final result of the fusion cross section of heavy-ion fusion reaction is independent of the choice of the absorption radius r_{abs}. It is due to the fact that in IWBC, there is strong absorption in the inner region and the incoming flux never returns. So, the expression of the fusion cross-section in Eq. (2.33) takes the form

$$\sigma_{fus} = \frac{\pi}{k^2}\sum_l 2(l+1)P_l(E) \tag{2.36}$$

where P_l(E) is the penetrability of the l-wave scattering. It is defined as

$$P_l(E) = 1 - |S_l|^2 = |T_l|^2 \tag{2.37}$$

Sudden limit approximation and constant coupling

In sudden limit approximation, the tunneling is assumed to occur much faster than the intrinsic motion, so that the nuclear structure is not perturbed during the penetration of the Coulomb barrier [21]. It is also called the 'adiabatic approximation'. In this case, the internal excitation energy is neglected with respect to the coupling interaction. This condition can be obtained from Eq. (2.29) by replacing $\epsilon_i \simeq 0$ in the M matrix. The new coupling matrix elements obtained are

$$M_{ij} \simeq < i|V_c(r,\zeta)|j > \tag{2.38}$$

The expression in the above equation is, however, valid only for strongly deformed nuclei [17].

The coupling potential can be factorized into two independent terms depending on the intrinsic term and the relative motion. However, it is assumed that the reduced mass and the potential energy are same for all the channels.

$$< i|V_c(r,\zeta)|j > \quad = \quad < i|F(r)G(\zeta)|j > \tag{2.39}$$

The main assumption of constant coupling approximation is that the form factors of all channels have the same radial dependence as F(r). In this case,

considering $F(r) = F(r_b)$, the value at the barrier where the coupling is stronger, a simplified equation is obtained as follows

$$\left[-\frac{\hbar^2}{2\mu}\frac{d^2}{dr^2} + V(r) - E \right]\phi_i(r) = -\sum_j M_{ij}\phi_j(r) = -F(r_b)\sum_i G_{ij}\phi_j(r) \tag{2.40}$$

The constant coupling approximation together with the sudden limit approximation allows the matrix to be diagonalized using a unitary transformation U which is independent of the relative distance r. The coupling matrix is diagonalized with respect to a base of eigenfunctions $\chi_j(r)$ with the associated eigenvalues λ_j.

$$\begin{aligned} \sum_i U_{ij}\phi_i(r) &= \chi_j(r) \\ \sum_{mn} U_{im}M_{mn}U^{+}_{nj} &= \delta_{ij}\lambda_j \end{aligned} \tag{2.41}$$

A system of decoupled differential equations of second order which satisfy the IWBC boundary conditions is obtained as follows:

$$\left[-\frac{\hbar^2}{2\mu}\frac{d^2}{dr^2} + V(r) + \lambda_i F(r) - E \right]\chi_i(r) = 0 \tag{2.42}$$

As can be seen in Eq. (2.42), the system can now be solved for a set of decoupled equations, each of which corresponds to a different inelastic channel i and is associated to a certain potential $V(r) + \lambda_i F(r)$. Hence, unlike in the case of one-dimensional model where a single Coulomb barrier exists, a spectrum of barriers $V(r) + \lambda_i F(r)$ is being dealt here. The transmission coefficient of each barrier is represented by $T_l(E, V(r) + \lambda_i F(r))$.

The total transmission coefficient is calculated as the weighted sum of the transmission coefficients.

$$T_l(E) = \sum_i |U_{il}|^2 T_l(E, V(r) + \lambda_i F(r)) \tag{2.43}$$

In the above equation $|U_{il}|^2$ represents the contribution of the i^{th} barrier to the fusion cross-section. It is represented by W_i and is calculated as

$$W_i = |U_{il}|^2 = |\, < i|l > \,|^2 \tag{2.44}$$

Hence the fusion cross-section is calculated as the weighted sum of the cross-sections of each channel.

$$\sigma^{fus}(E) = \sum_i W_i \sigma_i^{fus} \tag{2.45}$$

where σ_i^{fus} is the fusion cross-section of the i^{th} channel.

σ_i^{fus} corresponds to the expression of Eq. (2.10) in the case of one-dimensional model but with the new transmission coefficient.

$$\sigma_i^{fus}(E) = \sum_l \pi \lambda\!\!\!^{-2}(2l+1) T_l(E, V(r) + \lambda_i F(r)) \tag{2.46}$$

Iso-centrifugal approximation

There is also another approximation that allows to reduce the number of incoming channels and hence the dimension of the coupling matrix to be solved. It is called the 'iso-centrifugal approximation' [7, 21].

In the coupled channel model, when an excited state of internal spin I is coupled to the angular momentum l_i of the relative motion, $I+1$ channels are generated. Each orbital angular momentum of the type l_i'=$|l_i - I|, |l_i - I + 1|, .., |l_i + I|$ satisfies the condition $J = I + l_i$.

The assumption here is that the orbital angular momentum is the same in all reaction channels. This alternatively means the centrifugal potential is the same in all reaction channels. This assumption reduces the number of channels.

$$\frac{l_i(l_i+1)\hbar^2}{2\mu r^2} \approx \frac{J(J+1)\hbar^2}{2\mu r^2} \tag{2.47}$$

It is assumed that $l_i \approx J$, which means that the coupling of the spin I to the orbital angular momentum l is neglected. Therefore, there is only one effective channel for each excited state instead of $I+1$ channels.

2.2.2 Two channel problem

The coupled-channels model with the approximations can be easily understood with a simple two-level model. An entrance channel (labelled as 1) and an excited channel (labelled as 2) are considered with a coupling strength F as shown in Fig. 2.4.

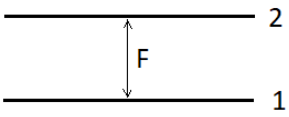

Figure 2.4: Coupling of entrance channel 1 and excited channel 2 with a coupling factor F

Inelastic channel with negligible Q-value

Assuming that the excited channel being dealt with is an inelastic channel and that the Q-value of the reaction is extremely small, simplified coupled channel equations are obtained as follow

$$\begin{aligned}\left[-\frac{\hbar^2}{2\mu}\frac{d^2}{dx^2}+V(x)-E\right]\chi_1 &= F(x)\chi_2\\ \left[-\frac{\hbar^2}{2\mu}\frac{d^2}{dx^2}+V(x)-E\right]\chi_2 &= F(x)\chi_1\end{aligned} \tag{2.48}$$

where χ_1 and χ_2 represent the wavefunctions of relative motion of the channels 1 and 2. Wavefunctions χ_+ and χ_- are introduced such that

$$\begin{aligned}\chi_+ &= \chi_1+\chi_2\\ \chi_- &= \chi_1-\chi_2\end{aligned} \tag{2.49}$$

The coupled channel equation in Eq. (2.48) can now be decoupled into the following equations

$$\begin{aligned}\left[-\frac{\hbar^2}{2\mu}\frac{d^2}{dx^2}+V(x)+F(x)-E\right]\chi_- &= 0\\ \left[-\frac{\hbar^2}{2\mu}\frac{d^2}{dx^2}+V(x)-F(x)-E\right]\chi_+ &= 0\end{aligned} \tag{2.50}$$

Satisfying the boundary conditions, it is obtained that

$$T(E) = T_1(E) + T_2(E) = \frac{T_+(E) + T_-(E)}{2} \tag{2.51}$$

which means that the total transmission coefficient can be easily expressed in terms of transmission coefficients calculated with the one-dimensional model.

The above result can be visualized in the figure below.

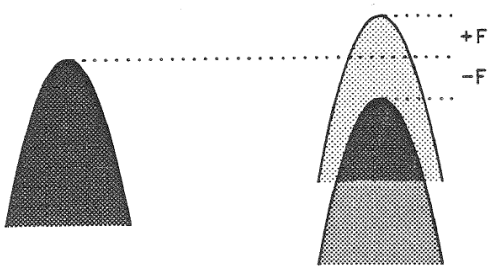

Figure 2.5: To the left is the potential barrier in the absence of coupling. To the right is the splitting of the potential barrier due to coupling [22]

As seen in Fig. 2.5, the potential barrier is split into two. One goes down by the amount of coupling factor F and the other goes up by the same amount. The effect of this split in the potential barrier on the transmission coefficient, in the classical picture, is shown in Fig. 2.6

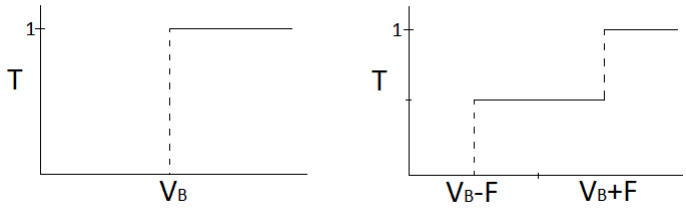

Figure 2.6: To the left is the transmission coefficient in the absence of coupling. To the right is the transmission coefficient after coupling [22]. V_B denotes the Coulomb barrier.

If the quantal effects are allowed, the transmission coefficient takes the following shape.

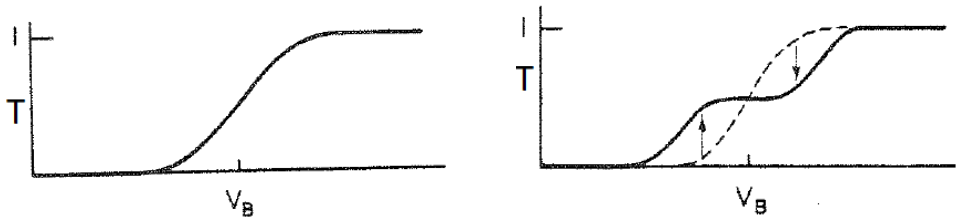

Figure 2.7: To the left is the transmission coefficient in the case of no coupling. To the right is the transmission coefficient after coupling [22].

From the above figure, it is clearly observed that the effect of coupling is to enhance the transmission coefficient for energies below the Coulomb barrier. At the same time, coupling decreases the transmission coefficient for energies above the Coulomb barrier.

Inelastic channel with finite Q-value

If the case is considered where the the excited channel is inelastic and has a finite Q-value, the decoupled equations take the form

$$\begin{aligned}\left[-\frac{\hbar^2}{2\mu}\frac{d^2}{dx^2}+V(x)+\lambda_- - E\right]\chi_- = 0\\ \left[-\frac{\hbar^2}{2\mu}\frac{d^2}{dx^2}+V(x)+\lambda_+ - E\right]\chi_+ = 0\end{aligned} \tag{2.52}$$

where $\lambda_\pm$ and $\chi_\pm$ are the eigenvalues and the eigenfunctions of the diagonalized coupling matrix, respectively.

For the system considered, the coupling matrix is

$$M = \begin{bmatrix} 0 & F \\ F & -Q \end{bmatrix}$$

Diagonalizing the coupling matrix, the following parameters are obtained

$$\begin{aligned}\lambda_\pm &= (-Q \pm \sqrt{4F^2+Q^2})/2\\ P_\pm &= \frac{F^2}{F^2+\lambda_\pm^2}\end{aligned} \tag{2.53}$$

where $P_{\pm}$ denotes the weights of the respective values $\lambda_{\pm}$. The result shows that the potential barrier is split into two. One goes up by λ_{+} and the other goes down by λ_{-}. In this case, there is asymmetrical splitting as shown in Fig. 2.8.

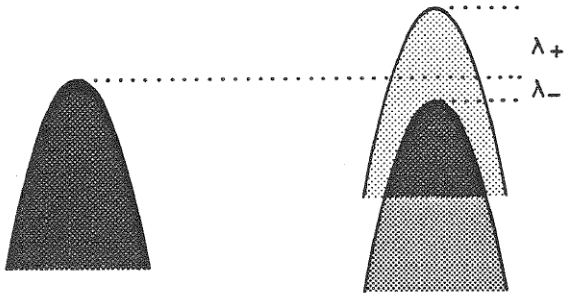

Figure 2.8: To the left is the potential barrier in the absence of coupling. To the right is the splitting of the potential barrier due to coupling [22], with finite Q-value.

The values of eigenvalues $\lambda_{\pm}$ and the weights $P_{\pm}$ as a function of Q-value is shown in the following figure. The values were calculated for a characteristic value of F = 1 MeV.

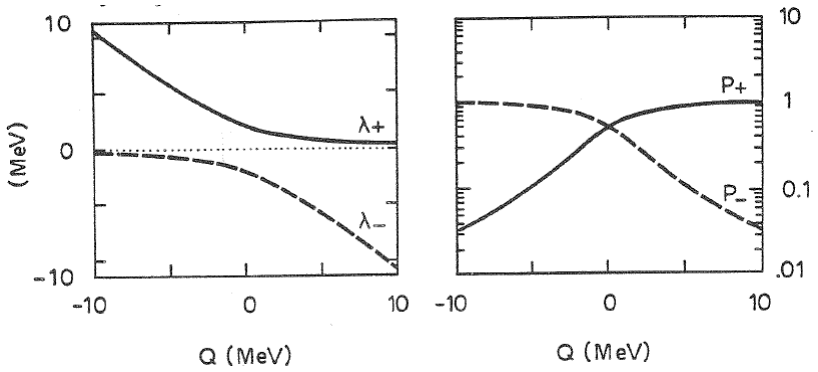

Figure 2.9: On the left (right) is the values of $\lambda_{\pm}$ ($P_{\pm}$) as a function of Q-value [22]

As observed in Fig. 2.9(left), there is always a barrier going down and therefore enhancement occurs at energies below the barrier. A complete picture is obtained by considering the weight factor $P_{\pm}$ in Fig. 2.9(right). For Q $<$ 0, small shift in λ_{-} is favoured by large value of P_{-} close to one. While in the case of

Q > 0, the potentially rich gain of a large value of λ_- is toned down by relatively low value of P_-.

2.2.3 CCFULL code

The CCFULL code is a program that calculates the fusion cross section and the angular momentum of the compound nucleus, taking into consideration the effect of couplings between the relative motion of the two interacting nuclei and intrinsic degrees of freedom on fusion [7]. The program takes into account all the channels relevant to the coupling in order to solve the coupled-channel equations numerically. The iso-centrifugal approximation is employed in order to reduce the dimension of the coupled-channel equations. It includes the couplings to full order without introducing the linear coupling approximation [7]. The finite excitation energies of intrinsic motions are taken into account. The program also includes Coulomb excitations and uses the IWBC inside the Coulomb barrier, thereby utilizing the minimum position of the Coulomb pocket inside the barrier, denoted by r_{min}.

Modified Numerov method [7] is used to directly integrate coupled second-order differential equations. For each partial wave, the barrier penetrability is calculated. Taking into account all the partial waves, the cross-section and the angular momentum of the compound nucleus are calculated as

$$\begin{aligned} \sigma^{fus}(E) &= \sum_J \sigma_J(E) = \pi \lambda\!\!\!^{-2} \sum_J (2J+1) T_J(E) \\ < l > &= \frac{\sum_J J\sigma_J}{\sum_J \sigma_J} \end{aligned} \tag{2.54}$$

Wood-Saxon parametrization of the nuclear potential is used, with no imaginary parts. The parameters are provided through an input file. The file contains the atomic number and mass number of the nuclei, the potential depth V_o, the radius R_o and the diffuseness a_o of the nuclear potential of the entrance channel.

Different kinds of inputs can be given to incorporate different couplings.

a) To include the vibrational coupling, for each level the excitation energy E_x, the deformation parameter β_λ, the multiplicity of the vibration coupling λ and the number of considered phonons n are also included in the input file.

The deformation parameter can be calculated using the relation:

$$\beta_\lambda^2 = \left(\frac{4\pi}{3Ze^2R^\lambda}\right)^2 4\pi B(E\lambda) \tag{2.55}$$

where $B(E\lambda)$ is the reduced transition probability of the electromagnetic decay from the excited state λ^π to the ground state, Z and R are the nuclear charge and radius respectively.

b) To take into account the pair transfer coupling, the inputs are provided with the Q-value of the transfer and the strength of the coupling.

c) In case of rotational coupling, the excitation energy of the first 2^+ state of the rotational band, the quadrupole deformation β_2 and the hexadecapole β_4 deformation parameters and the number of levels in the band have to be included in the input file.

Excitations of surface mode

The coupling of the surface excitation states of a nucleus is caused by the interaction V(r - δR). V(r) denotes the ion-ion potential and the surface distortion δR is given by

$$\delta R = \sum_{n\lambda\mu} R\alpha_{n\lambda\mu} Y_{\lambda\mu}(r) \tag{2.56}$$

where $\alpha_{n\lambda\mu}$ denotes the static or dynamic deformation amplitude.

If the nuclei collide along the z-axis, in the rotating frame, the value of μ=0. The surface distortion can be simplified as

$$\delta R = \sum_{n\lambda} R\alpha_{n\lambda 0} \sqrt{\frac{2\lambda+1}{4\pi}} \tag{2.57}$$

This condition allows to define the matrix element of the surface distortion amplitude between the ground state and the first excited state.

$$< n\lambda|\delta R|00 >= \frac{\beta_{n\lambda} R}{\sqrt{4\pi}} \tag{2.58}$$

The above expression is valid for both static and dynamic deformations, i.e. rotational and vibrational excitations. Both nuclear and Coulomb potentials can be derived using the deformation parameter .

For the Coulomb interaction, a first-order approximation is enough and the non-diagonal elements of the coupling matrix are expressed as

$$\delta V_C = \sum_n \frac{3Z_1Z_2e^2}{2\lambda+1}\frac{R^\lambda}{r^{\lambda+1}}\alpha_{n\lambda 0}\sqrt{\frac{2\lambda+1}{4\pi}} \tag{2.59}$$

In the case of nuclear interaction, the non-linear couplings significantly affect the shape of fusion barrier distributions [23]. Using the CCFULL code, coupling of the surface excitations to all orders can be calculated [24].

$$\begin{aligned} U(r-\delta R) &\sim U(r) + \delta V_N \\ \delta V_N &= -\frac{dU}{dr}\delta R + \frac{1}{2}\frac{d^2U}{dr^2}[(\delta R)^2 - <0|(\delta R)^2|0>] \end{aligned} \tag{2.60}$$

The CCFULL code is suitable for dealing with both light and heavy ion fusion, where multiple excitations are taken into account with great importance. The low energy states 2^+ and 3^- are the main excitations that influence the heavy ion fusion reactions.

Vibrational coupling

In the CCFULL code, the vibrational coupling is considered by parameterization of the vibrational potential through a harmonic oscillator. A dynamic operator which depends on the creation operator $a^+_{\lambda 0}$ and the annihilation operator $a_{\lambda 0}$ of phonons is introduced. This operator is added to the radius parameter of the Wood-Saxon potential.

$$R_{00} + \hat{O} = R_0 + \frac{\beta_\lambda}{\sqrt{4\pi}}R_t(a^+_{\lambda 0} + a_{\lambda 0}) \tag{2.61}$$

wher β_λ is the deformation parameter, λ is the multipolarity and R_t is the radius of the target.

R_t is expressed as a function of the coupling radius r_{cp} as

$$R_t = r_{cp}A_t^{1/3} \tag{2.62}$$

The matrix element between the n-phonons $|n>$ state and m-phonons $|m>$ is

$$\hat{O}_{nm} = <n|\hat{O}|m> = \frac{\beta_\lambda}{\sqrt{4\pi}}R_t(\sqrt{m}\delta_{n,m-1} + \sqrt{n}\delta_{n,m+1}) \tag{2.63}$$

The elements of the nuclear potential matrix can be derived by diagonalizing the dynamic operator $\hat{O}$ as follows

$$V^N_{nm} =< n|V^N(r,\hat{O})|m > -V^N_0\delta_{n,m} \tag{2.64}$$

where the term $V^N_0\delta_{n,m}$ makes sure that there is no double counting of the same term in the diagonal components.

However, for the coupling of the Coulomb potential with the vibrational degrees of freedom the code employs linear coupling approximation. The matrix element V^C_{nm} is added to the nuclear element V^N_{nm}.

$$V^C_{nm} = \frac{\beta_\lambda}{\sqrt{4\pi}}\frac{3}{2\lambda+1}Z_PZ_Te^2\frac{R^\lambda_T}{r^{\lambda+1}}(\sqrt{m}\delta_{n,m-1} + \sqrt{n}\delta_{n,m+1}) \tag{2.65}$$

In realistic cases, the intrinsic motion deviates from the harmonic limit, even when the levels are equally spaced and the electromagnetic transitions do not alter the linear approximation. Still, the adopted matrix formalism provides a convenient and useful technique to evaluate the coupling matrix elements.

Rotational coupling

Coupling with the rotational excitation states is included in the case of deformed nuclei. A dynamical operator $\hat{O}$ is used to change the target radius in the nuclear potential.

$$R_{00} + \hat{O} = R_0 + \beta_2R_tY_{20} + \beta_4R_tY_{40} \tag{2.66}$$

where β_2 and β_4 are the the quadrupole and hexadecapole deformation parameters of the deformed target nucleus respectively. R_t is defined as a function of the coupling radius r_{cp}, $R_t = r_{cp}A^{1/3}_t$ as in Eq. (2.62).

In order to calculate the matrix elements of the coupling Hamiltonian between the $|n >= |I0 >$ and $|m >= |I'0 >$ states of the ground state rotational band of the target, the dynamical operator is diagonalized. The obtained matrix elements are shown below

$$\hat{O}_{II'} = \sqrt{\frac{5(2I+1)(2I'+1)}{4\pi}}\beta_2R_t\begin{bmatrix} I & 2 & I' \\ 0 & 0 & 0 \end{bmatrix}^2 + \sqrt{\frac{9(2I+1)(2I'+1)}{4\pi}}\beta_4R_t\begin{bmatrix} I & 4 & I' \\ 0 & 0 & 0 \end{bmatrix}^2 \tag{2.67}$$

These elements are introduced into the potential representation. The coupling matrix elements of nuclear potential can now be expressed as

$$V^N_{nm} =< n|V^N(r,\hat{O})|m > -V^N_0\delta_{n,m} = \sum_\alpha < I0|\alpha >< \alpha|I'0 > V^N(r,\lambda_\alpha) - V^N_0\delta_{n,m} \tag{2.68}$$

For the Coulomb interaction of the deformed target, second order of β_2 and first order of β_4 are included. The higher couplings of the Coulomb interaction play a minor role.

$$\begin{aligned} V^C_{nm} =& \frac{3Z_PZ_T}{5}\frac{R^2_T}{r^3}\sqrt{\frac{5(2I+1)(2I'+1)}{4\pi}}(\beta_2 + \frac{2}{7}\sqrt{\frac{5}{\pi}}\beta^2_2)\begin{bmatrix} I & 2 & I' \\ 0 & 0 & 0 \end{bmatrix}^2 + \\ & \frac{3Z_PZ_T}{9}\frac{R^4_T}{r^5}\sqrt{\frac{9(2I+1)(2I'+1)}{4\pi}}(\beta_4 + \frac{9}{7}\beta^2_2)\begin{bmatrix} I & 4 & I' \\ 0 & 0 & 0 \end{bmatrix}^2 \end{aligned} \tag{2.69}$$

Sum of V^N_{nm} and V^C_{nm} gives the total coupling matrix element.

Transfer coupling

The influence of transfer processes on the fusion reactions at sub-barrier energies has been observed. There are evidences of enhancement of the cross sections with respect to the CC calculations including the coupling to the vibrational and rotational states. Therefore, the coupling of the pair-transfer between the ground states of the interacting nuclei is included in the CC calculation. This is achieved by including a macroscopic form factor [10].

$$F_{trans}(r) = F_t\frac{dV^N_0}{dr} \tag{2.70}$$

where F_t is the coupling strength.

2.3 Enhancement and Hindrance

It is evident that there is enhancement of the fusion cross-section for heavy ion reactions at energies above and below the Coulomb barrier due to coupling of reaction channels. However, recent studies at deep sub-barrier energies show that the CC calculation overestimated the fusion cross-section at deep sub-barrier energies for a number of systems. The experimental data show a steeper drop in the fusion cross-sections at deep sub-barrier energies. This phenomenon is called "hindrance effect". It is an effect that opposes the enhancement of fusion cross-section at very low sub-barrier energies.

One of the first evidences was observed in the fusion cross-section measurement of ^{64}Ni+^{64}Ni [16, 25]. The drop in the experimental fusion cross-section (black dots) from the standard CC calculation (dashed line) is clearly observed in Fig. 2.10 (a).

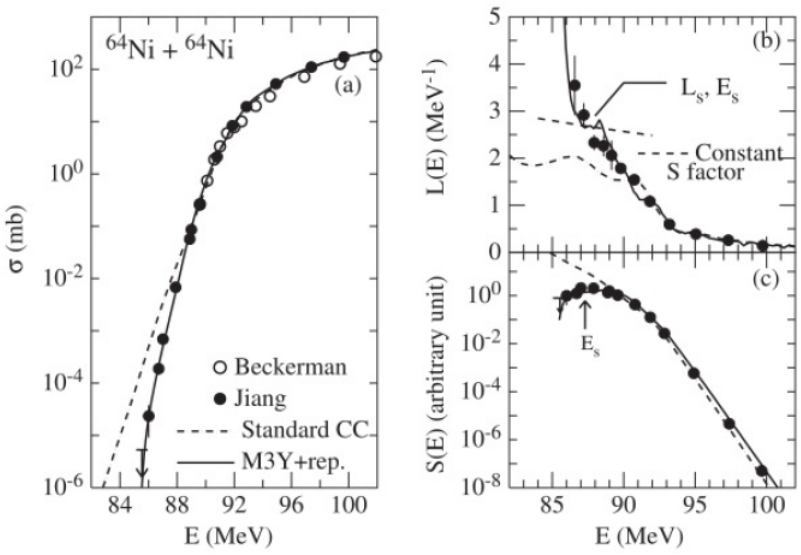

Figure 2.10: (a) Excitation function, (b) logarithmic derivative L(E) and (c) astrophysical S factor S(E) [26] of the system ^{64}Ni + ^{64}Ni [16, 25] , where hindrance was observed.

There are two models proposed in order to explain the fusion hindrance at deep-subbarrier energies: a) adiabatic approach model and b) sudden approach model. The two models, even though differ a lot in explaining the origin of hindrance, reproduce several experimental data equally well.

a) The "adiabatic approach model" has been proposed by Ichikawa et al. [27]. According to this model, there is a neck formation between the colliding nuclei in the overlap region (see Fig. 2.11) and the fusion occurs through it. The fusion occurs in the time required for the density distribution to adjust to the optimal distribution. Whereas, the origin of hindrance lies in the tunneling of a one-body potential due to the neck formation.

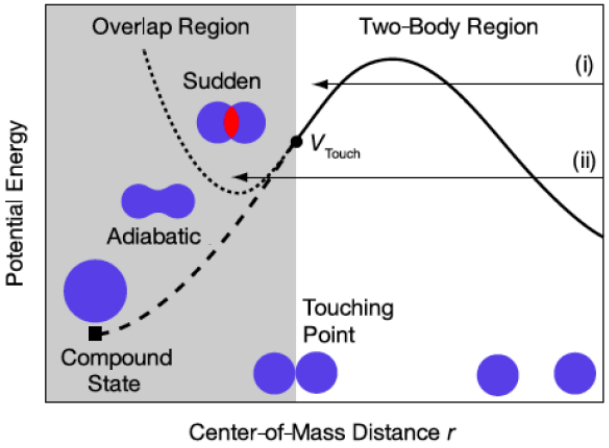

Figure 2.11: Scheme of a heavy ion-ion potential as a function of the center-of-mass distance r between colliding nuclei [28]

b) The "sudden approach model" has been proposed by Misicu and Esbensen [29, 30]. In this model, the nuclei density is treated as frozen during the collision suggesting that fusion occurs rapidly. It is suggested that the incompressibility of nuclear matter becomes effective at small internuclear distances which generates a repulsive core in the ion-ion potential. This creates a potential which is much shallower than standard potentials (see Fig.2.11). This causes the hindrance in the fusion reaction.

Logarithmic slope and Astrophysical S-factor

The appearance of hindrance can be highlighted using two model-independent representations of the experimental cross-sections: logarithmic slope L(E) and astrophysical S-factor S(E).

The logarithmic derivative of the energy-weighted cross section L(E) represents the slope of the excitation function[4]. The expression is

$$L(E) = \frac{d[ln(E\sigma)]}{dE} = \frac{1}{E\sigma}\frac{d(E\sigma)}{dE} \tag{2.71}$$

where E is the energy in the center of mass system.

As seen in Fig. 2.10 (right), the value of L(E) rises as the energy decreases.

The astrophysical S-factor is a very important quantity widely used in the study of nuclear astrophysics [31]. It is calculated as:

$$S(E) = E\sigma(E)e^{2\pi(\eta-\eta_o)} \tag{2.72}$$

where E is the energy in centre of mass frame and η is the Sommerfeld parameter.

$$\eta = 0.157\frac{Z_pZ_t}{\sqrt{E/\mu}} \tag{2.73}$$

where Z_p and Z_t are the atomic numbers of the projectile and the target respectively and η_o is a convenient scaling factor.

Since the S-factor is directly extracted from the cross sections, it provides a very useful way of representing the trend of the excitation function in the sub-barrier region. The two quantities L(E) and S(E) are related algebraically as

$$\frac{dS(E)}{dE} = S(E)\left[L(E) - \frac{\pi\eta}{E}\right] \tag{2.74}$$

The S-factor has a maximum when $\frac{dS(E)}{dE} = 0$ i.e.,

$$\begin{aligned} S(E)\left[L(E) - \frac{\pi\eta}{E}\right] &= 0 \\ \Rightarrow L(E) = L_{CS}(E) &= \frac{\pi\eta}{E} \end{aligned} \tag{2.75}$$

which means that the S-factor shows a maximum at the energy where the logarithmic slope is equal to L_{CS}. This value of energy E_s is referred to as the threshold of hindrance effect.

Observing the hindrance effect through the trend of the S-factor may sometimes be difficult when no maximum in the S-factor is observed for the energy range where measurements were made. Comparison of the experimental data with the standard CC calculation is necessary in such cases. A drop in the measured fusion cross-section with respect to the CC calculations at low energies indicates the presence of hindrance.

Chapter 3

Study of $^{12}C+^{24}Mg$: motivations

3.1 Choice of the system

Fusion reactions between light heavy ions play a prominent role in the dynamics of stellar evolution [6]. Light systems such as $^{12}C+^{12}C$, $^{12}C+^{16}O$ and $^{16}O+^{16}O$ are very important for the evolution of massive stars [5], beyond the burning of helium and the associated nucleosynthesis. The existence of hindrance in these systems would lead to significant changes in the abundances of several isotopes and their formation. Also, there will be an increase in the ignition temperature of $^{12}C+^{12}C$ which is a very important reaction that occurs in the quiescent C burning in massive stars and in the explosive C burning in collapsing white dwarfs, eventually leading to thermonuclear supernovae.

Several studies have been made on the fusion cross-sections of $^{12}C+^{12}C$ and $^{12}C+^{16}O$. Fusion cross-section study of $^{12}C+^{16}O$ showed a decreasing trend of S-factor [32]. This could be a possible hint to the presence of hindrance effect in the light systems. But these measurements in the light systems often have large uncertainties and there are serious differences between the results of different experiments in the very low energy range relevant for astrophysics.

The closest possible approach is to study the detailed low energy behaviour for medium-light systems slightly heavier than the mentioned reactions involving e.g., fusion of carbon and oxygen nuclei [33]. It is quite positive that these results will provide the guidelines to extrapolate the behaviour to systems of astrophysical

importance.

Therefore, ^{12}C+^{24}Mg was chosen for fusion cross-section studies at energies near and below the Coulomb barrier. The system also provides a link between light heavy ion systems and the heavier systems studied in recent years such as ^{12}C+^{30}Si [6] reaction.

3.2 Physical motivation

Hindrance has been recognized as a general phenomenon in medium-heavy-mass systems. In this mass region, the fusion Q-value is always negative. As a consequence of conservation of energy, the value of S approaches 'zero' as the value of incident energy approaches E = -Q. Under such conditions, a maximum in the S-factor is unavoidable [34].

The light systems of astrophysical importance and near-by systems have positive Q-values. Whether there is also an S-factor maximum at very low energies for these systems is an experimentally challenging question. Some studies of systems with medium to light masses with positive Q-values have been performed at LNL and other laboratories, but a firm existence of S-factor maximum has not been established so far.

A recent study was made for the system ^{12}C+^{30}Si (Q_{fus}= +14.11 MeV) in inverse kinematics at LNL [6]. The results are briefly discussed in sub-section 6.1. Even though the evidence was not conclusive, the S-factor seemed to indicate a maximum around 10.5 MeV.

The success of the inverse-kinematics study of ^{12}C+^{30}Si opened the possibility to perform fusion cross-section measurement of ^{12}C+^{24}Mg (Q_{fus}= +16.3 MeV) to study the hindrance at deep sub-barrier energies. The compound nucleus formed is ^{36}Ar which is six mass units lower than ^{42}Ca, formed in the case of ^{12}C+^{30}Si.

The 'system parameter' or 'entrance channel parameter' of a system governs behavior of the system. It is defined as

$$\zeta = Z_1 Z_2 \sqrt{\mu} \tag{3.1}$$

where Z_1 and Z_2 are the atomic numbers of the two colliding nuclei and μ is the reduced mass.

The value of ζ for the systems $^{12}C+^{12}C$, $^{12}C+^{16}O$, $^{12}C+^{24}Mg$ and $^{12}C+^{30}Si$ are 88.2, 181.0, 203.6 and 245.9, respectively. The close similarity between $^{12}C+^{24}Mg$ and lighter systems is then obvious.

A new simple formula, using only three parameters, to calculate the fusion excitation function has been developed by C.L. Jiang et al. [35] recently. Least-square fitting have been performed on the excitation functions of $^{16}O+^{18}O$ and $^{12}C+^{30}Si$ to extract the parameters. These parameters were used to obtain the interpolated parameters for $^{12}C+^{24}Mg$ system. The calculations using the interpolated parameters very well describes the previous measurements [36, 37] of $^{12}C+^{24}Mg$ excitation function at high energies as shown in Fig. 3.1.

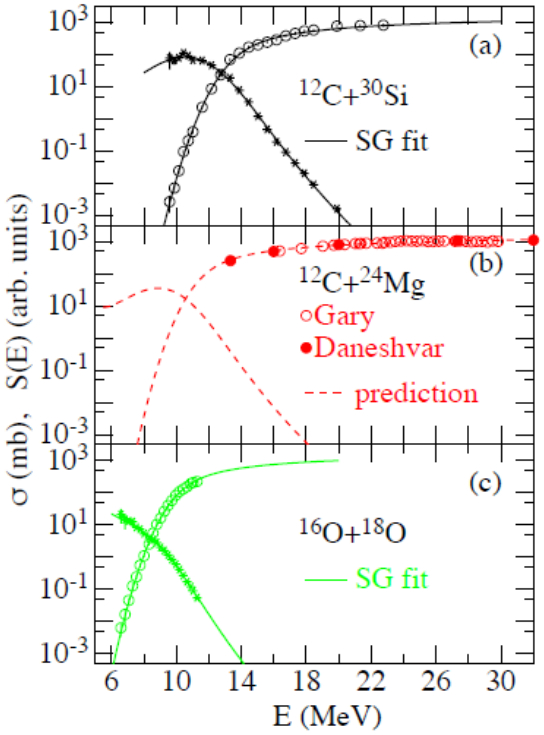

Figure 3.1: Least square fitting of $^{12}C+^{30}Si$ (a) and $^{16}O+^{18}O$ (c). Predictions for $^{12}C+^{24}Mg$ (b) using the interpolated three parameters [35].

According to the calculation, at low energies an S-factor maximum is predicted at threshold cross-section around 0.1 mb. Observation of hindrance effect in this system would strongly support that hindrance effect is a general phenomenon in lighter systems too.

Chapter 4

Set-up and experimental procedure

Even if this thesis work has concerned the data analysis and the theoretical interpretation of the fusion excitation function of $^{12}C+^{24}Mg$, a short description of the experimental set up previously used for the experiment, is given here below.

The experimental measurement of fusion cross-section can be done by direct detection of evaporation residues (ER) or by the detection of characteristic gamma-rays or light particles evaporated during the de-excitation of the compound nucleus. Even though the direct detection of ER is the most accurate method, it requires addressing various technical problems and is very challenging. Electric and/or magnetic fields are employed to physically separate the ER, which are forward peaked, from the direct beam and the intense flux of the elastically scattered beam particles at small angles. The perpendicular electrostatic field efficiently separates the beam from the ER, by exploiting the difference in electrical rigidity between ER and beam or beam-like particles.

Fig. 4.1 shows the PISOLO set-up installed in Laboratori Nazionali di Legnaro (LNL). PISOLO is an electrostatic deflector used to study fusion dynamics above and below the Coulomb barrier via direct detection of ER events produced with stable beams. The set-up allows fast and reliable measurements of of relative and absolute fusion cross-sections. The main components are a reaction chamber, an electrostatic deflector, an energy and energy loss-time of flight telescope based on micro-channel plates, an ionization chamber and a silicon surface barrier detector.

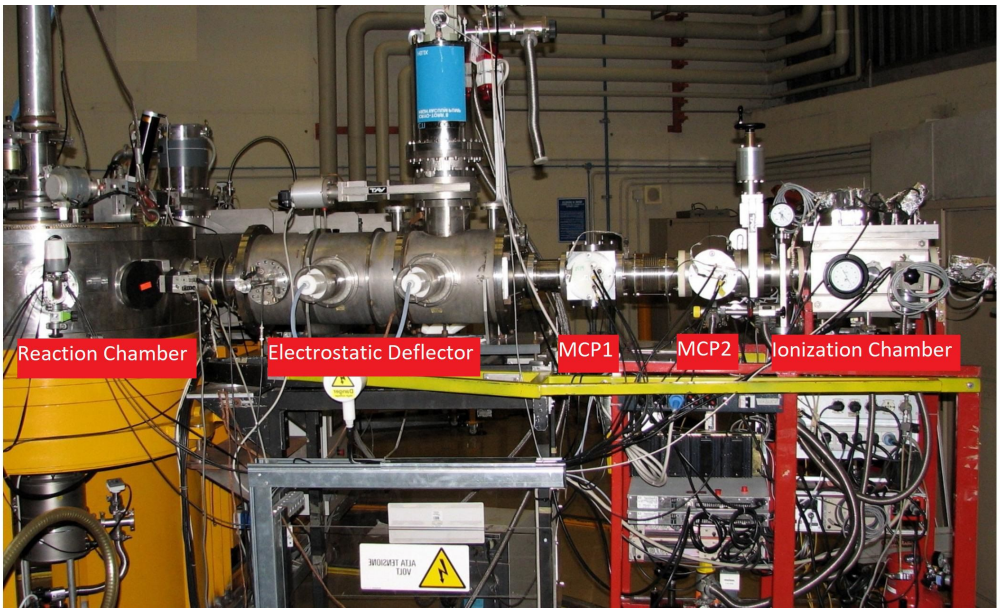

Figure 4.1: Experimental set-up of PISOLO.

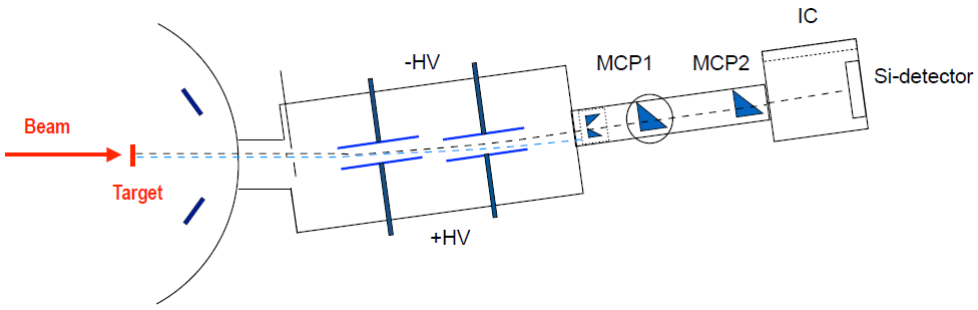

Figure 4.2: Horizontal view of the set-up. From the left: reaction chamber, electrostatic deflector and TOF-ΔE-E telescope.

4.1 Scattering chamber and electrostatic deflector

The scattering chamber allows a rotation that keeps the vacuum inside (10^{-6}mbar) by means of a sliding seal which aids to perform angular distribution measurements. The chamber is a stainless steel cylinder with an internal radius of 50 cm. A target support is attached to the upper cover of the chamber to hold the

six-position holder (see Fig. 4.3 left) where the targets are fixed. In one position a quartz plate is mounted, with a small central hole (1.5 mm in diameter). The support can be moved through an external control system to enable focusing of the beam at each change of energy and also to change the target or its angle with respect to the beam direction.

To normalise the fusion yields to the Rutherford scattering cross-section and to monitor the changes in the beam position on the target, four monitors are used. These monitors are silicon detectors, each of 50 mm^2, placed at a variable distance from the target. Normally the distance is 195 mm corresponding to a detection angle of $\theta_{lab} = 16.1^o$ with respect to the beam line. The monitors are mounted on a circular support (see Fig. 4.3 right). The monitors have collimators with a diameter of 1.5 mm which reduces the counting rate and hence the radiation damage. The total solid angle for the four monitors is calculated to be $\Delta\Omega_{mon} = (166.7 \pm 1.7)$ μsr.

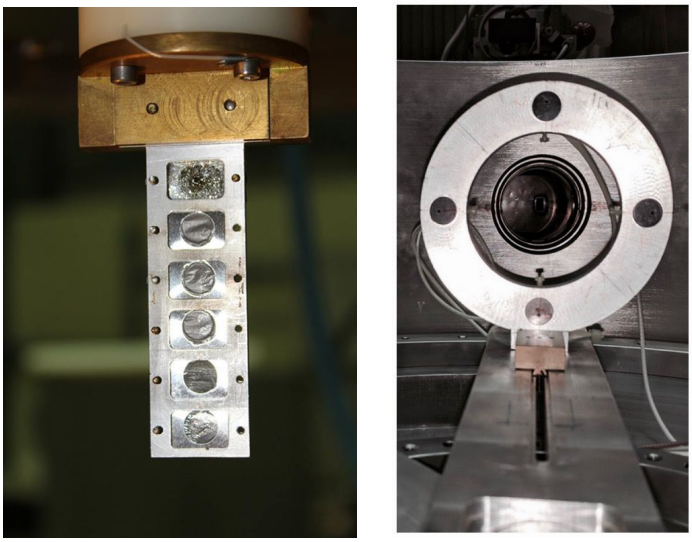

Figure 4.3: The target holder (left) and the four monitors (right)

The use of an electrostatic deflector is important to separate the ERs from the residual beam as the maximum of the ER differential cross-section is found in a narrow peak centred at 0^o, with a FWHM of few degrees. The separation is

based on the difference of the electrical rigidity which is defined as

$$\eta = \frac{E}{q} \tag{4.1}$$

where E is energy and q is the ion charge state.

The deflector is placed at an angle of 4.7^o with respect to the beam direction. The trajectory of the charged particles is governed by the relation between centrifugal force and electrostatic force:

$$\frac{mv^2}{r} \approx q\epsilon \tag{4.2}$$

where v and m are the velocity and the mass of the ion respectively while ϵ is transverse electric field and r is the radius of curvature. At a deflection angle being considered, the trajectory of charged particles in the electrostatic field region can be well approximated to an arc of radius r.

Figure 4.4: The internal part of the electrostatic deflector with the two pairs of electrodes (left) and the used MCP (right).

Considering that the momentum of ER and the beam particles are approximately equal, by the law of conservation of momentum, the ratio between the radii of curvatures of the residues(r_{ER}) and of the beam particles(r_b) is proportional to the respective electrical rigidities.

$$\frac{r_{ER}}{r_b} \approx \frac{\Big(E/q\Big)_{ER}}{\Big(E/q\Big)_b} \approx \frac{\Big(mq\Big)_b}{\Big(mq\Big)_{ER}}$$

The evaporation residues have more pronounced curvature as the mass and charge state of the evaporation residues are usually greater than those of the beam. These difference in trajectories gives a clear separation between the evaporation residues and the beam, even for measurements performed at 0^o.

The electrostatic deflector is placed inside a stainless steel cylinder of diameter 30 cm and length 85 cm, see Fig. 4.4 (left). Two pairs of stainless steel rectangular electrodes with smooth surface are placed inside the cylinder. Each electrode has dimensions of 25 cm x 12 cm and a thickness of 0.5 cm. The distance between the plates is externally adjustable and separately for each electrode. There are two different and independent field regions which allow a good adjustment for the different experimental conditions by minimizing the scattering of the beam on the plates. The electrodes are connected to two high voltage power supplies which allow them to reach a maximum voltage of about 40 kV. A collimator is placed between the reaction chamber and the electrostatic deflector (entrance collimator) and it defines the acceptance angle of the deflector.

The applied voltage along with the geometry of the deflector plates bend slightly the primary beam that is stopped on a side of the collimator (exit collimator) which is placed at the end of the deflector. As the evaporation residues have lower electrical rigidities, they pass through the collimator and reach the detection system. The ratio of the number of evaporation residues that exits to that enters the electrostatic deflector defines the transmission efficiency of the electrostatic deflector.

To ensure the maximum transmission of the residues, an appropriate applied voltage is chosen. However, not all the primary beam is stopped. A 'rejection factor' is defined as the ratio between the number of incoming and outgoing beam particles from the deflector. For a typical fusion system, the rejection factor is $\simeq 10^{7-8}$, according to the beam energy. Following the scattering in the target and the multiple collisions with the electrodes or the edges of the collimators, a fraction of the beam particles which is degraded in energy enters the exit collimator. Therefore, a further separation of the two types of ions is necessary which is realized by the detector telescope downstream of the exit collimator.

4.2 Detector telescope

The telescope consists of two micro-channel plates detectors (MCP), a ionization chamber (IC) and a heavy-ion partially depleted silicon surface barrier detector inside the ionization chamber.

The time of flight (TOF) is measured with the two MCPs together with the the silicon detector. The two flight bases are 666 mm and 1047 mm. The time of flight between the first (second) MCP and the silicon detector is referred to as TOF1(TOF3). The time of flight between the two MCPs is referred to as TOF2.

For the same kinetic energy, the more massive particles have longer time of flight with respect to the lighter particles. The telescope exploits this difference in the time of flight to discriminate the beam particles and the evaporation residues. The time of flight is related to the mass by the relation:

$$\begin{aligned} E &= \frac{mv^2}{2} \\ &= \frac{md^2}{2TOF^2} \\ \Rightarrow TOF^2 &= \frac{md^2}{2E} \\ \Rightarrow TOF &= d\sqrt{\frac{m}{2E}} \end{aligned} \tag{4.3}$$

where E is the kinetic energy of the particle, m is the mass of the particle, d is the flight length and TOF is the time of flight.

The evaporation residues have higher masses than the beam particles and hence have longer time of flight through the telescope. This allows to distinguish between the evaporation residues and the beam particles by measuring their time of flight (TOF) and their energy E.

The mass resolution can be derived from Eq. (4.3) by expressing the mass as a function of energy and TOF as follow:

$$\begin{aligned} m &= \frac{2E.TOF^2}{d^2} \\ \Rightarrow \left(\frac{\Delta m}{m}\right)^2 &= \left(\frac{\Delta E}{E}\right)^2 + 4\left(\frac{\Delta TOF}{TOF}\right)^2 \end{aligned} \tag{4.4}$$

The relative error on the time of flight TOF can be reduced by increasing the flight length at the expense of the solid angle.

The MCPs have time resolution comparable to the silicon detectors and overall they sum up to around 300 ps. The time resolution is $\Delta TOF/TOF \sim 0.7\%$. This is comparable to the energy resolution of $\Delta E/E \sim 1\%$. Therefore the mass resolution is around $\Delta m/m \sim 1/60$ in typical cases.

After passing through the MCPs, the particles pass through an ionization chamber before reaching the silicon detector. The ionization chamber provides the differential energy loss of the particles. The particles then reach the silicon detector which measures the residual energy and at the same time provides both the trigger for data acquisition and the start signal for the time of flights.

The telescope and the deflector are mounted on a platform which can be rotated in order to perform angular distribution measurements. When the detection system is placed at 0^o the deflector is tilted by 4.7^o with respect to the beam line whereas the telescope is shifted by 47 mm with respect to the symmetry axis of the deflector. This is the typical configuration employed in fusion reaction studies.

Micro Channel Plates detectors

The use of MCP detectors is required for the detection of low-energy heavy ions without significantly altering their energy [38].

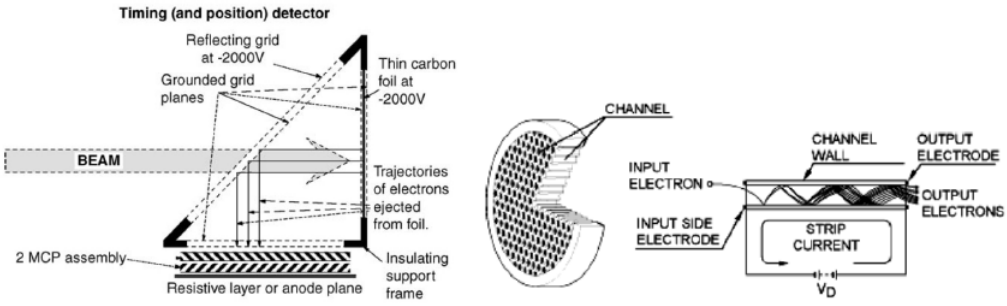

Figure 4.5: Scheme of a MCP detector with electrostatic mirror [39] (on the left) and of a MCP plate (on the right).

The MCP detectors are based on $43\times63 mm^2$ glass plates especially designed to act as very compact electron multipliers with high gain (around 10^3). In the installed MCP detectors two glass plates are mounted in chevron configuration to

get a fast time signal as output which is large enough for further processing, see Fig. 4.5. An overall gain of the order of 10^6 is achieved with the two glass plates. A high vacuum condition ($10^{-5} - 10^{-6}$ mbar) is required for their operation.

The ions do not collide directly on the plates. They pass through a thin carbon foil of about 20 μg/cm^2 placed perpendicularly to their direction. The ion-carbon interaction is followed by the emission of delta-electrons. These electrons are successively accelerated and bent onto the plates by a 45^o electrostatic mirror, where a voltage of about 1 kV is applied. A metallic anode is used to collect the electrons produced. The process generates negative output signals with amplitudes of 10-100 mV or more which depends on the ions and on their energy, and a rise time of few nanoseconds.

The geometry of the detectors guarantees the isochronism of the signals generated by the electrons, independent of the crossing point in the carbon foil. Each MCP detector has a transparency of 85%, due to the presence of several grids. For the heavy ions, their measured intrinsic efficiency is close to 100%.

Ionization Chamber

Ionization chambers are basically gas-filled detectors. It is a linear detector which collects all the charges created by the direct ionization within the gas through the application of an electric field. It only uses the discrete charges created by each interaction between the incident radiation and the gas, and does not involve the gas multiplication mechanisms. The electrical signal developed by the ionization chamber is basically constituted by the total number of ion pairs created along the radiation track. It also depends linearly on the energy the particle has lost in the gas volume of the chamber. The energy required to create an ion pair is independent of the particle's energy and has a fixed mean value of about 30 eV for CH_4.

The ionization chamber in PISOLO used a Frisch grid [40]. It has been used for several fusion reaction measurements with stable beams. An electric field perpendicular to the beam is generated by two parallel electrodes. This transverse electric field gives the advantage of fast separation of the formed ion pairs from the beam line. A single plate of stainless steel is used as a cathode. However,

the anode is segmented into three parts of 8 cm, 6cm and 14 cm, which allows to measure three differential energy loss signals to enable particle identification. The three energy losses are, however, combined into a single total energy loss signal in normal working condition.

For fusion reaction studies, the pressure is typically few mbar and up to 20-30 mbar. The pressure is so chosen that the evaporation residues lose about half of their energy in the gas. The applied voltage is then chosen to maximize the electron drift velocity. The applied voltage is about 300V in typical working condition. The separation between the electrodes is 10 cm and so the transverse electric field is about 3000 V/m. In the ionization chamber, methane CH_4 is normally used. Despite the interactions with crossing ions and the impurities that may be produced by the walls and various components of the circuit, the purity of the gas needs to be assured and hence, it is kept flowing during the measurements. Another advantage provided by the flow of the gas is that it reduces the recombination and provides a good energy resolution.

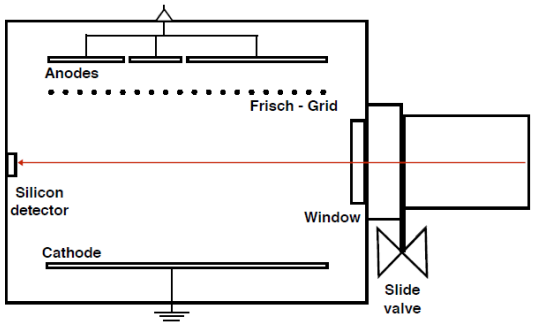

Figure 4.6: Scheme of the transverse field IC with Frisch grid of the PISOLO set-up.

As can be seen in Fig. 4.6, a thin Mylar window of 200 μg/cm^2 is placed at the entrance of the ionization chamber. The beam ions and the evaporation residues pass through this window to enter the ionization chamber. The particles then pass through the gas and later, are stopped in the silicon detector of surface area 600 mm^2 and 100 μm thickness. The silicon detector provides a signal proportional to their residual energy.

However, for the experiment performed, a different ionization chamber was

used in order to have a higher counting rate and faster response. This particular ionization chamber is well-described in the PhD thesis of Giulia Colucci [26]. A schematic of the ionization chamber used is shown below:

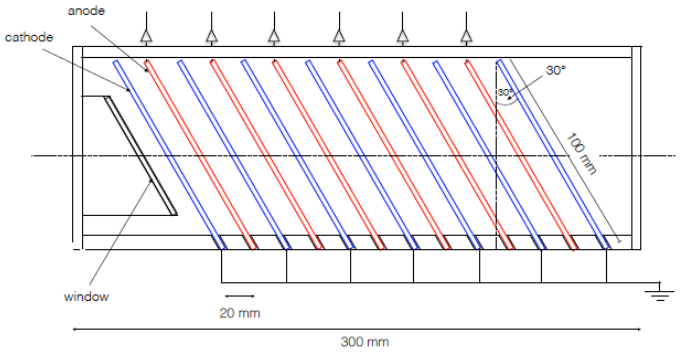

Figure 4.7: Scheme of the fast ionization chamber used [26].

Time of flight as a function of the energy provided by the silicon detector is shown in Fig. 4.8 (left panel). Also time of flight as a function of the energy loss provided by the IC is shown in Fig. 4.8 (right panel). The reaction studied was ^{12}C+^{30}Si in inverse kinematics [6]. In this case, the evaporation residues (ER) are well identified and separated from the degraded beam.

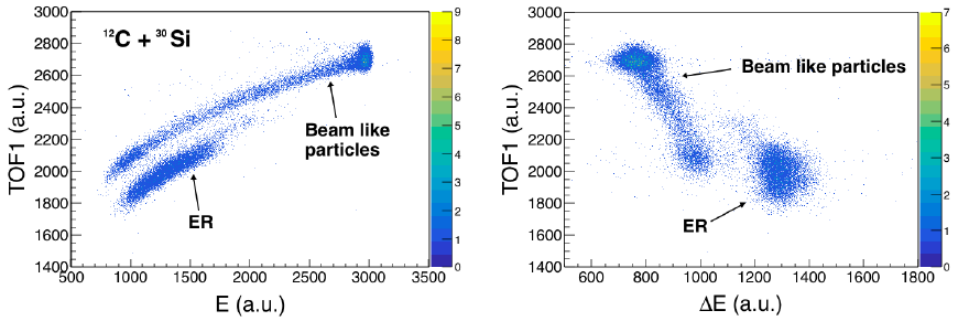

Figure 4.8: Time of flight TOF1 vs. residual energy (left) and TOF1 vs. the energy loss (right), measured for ^{12}C+^{30}Si in inverse kinematics [6]. The energy of the ^{30}Si beam was 51 MeV, which is above the Coulomb barrier of the system.

4.3 Electronics and acquisition system

The scheme of the electronics used for processing the signals from the monitors, MCPs, IC and Si detector is shown in Fig. 4.9.

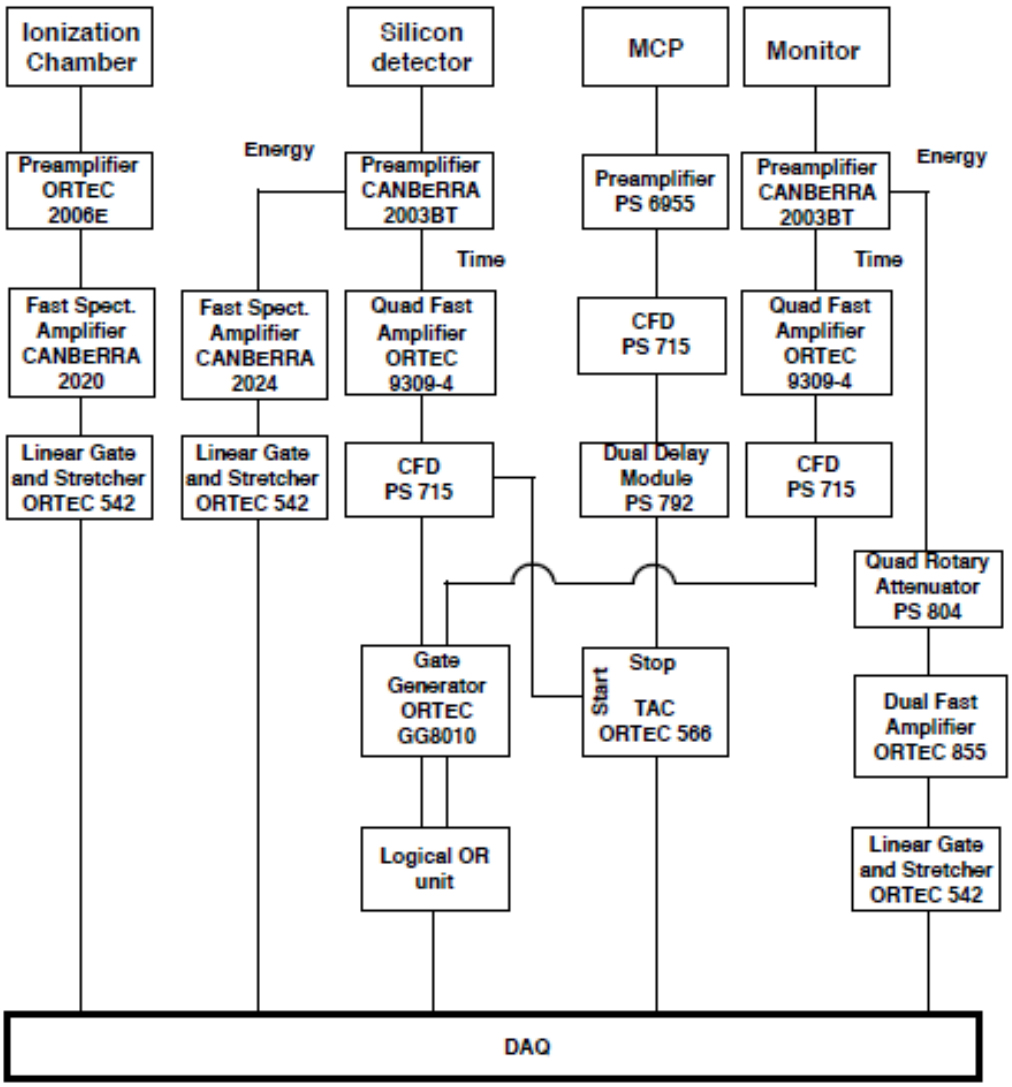

Figure 4.9: Electronic chain of the monitors, MCPs, IC and Si detector [26].

Most of the electronic chain is built up using standard NIM modules, due to the limited number of the parameters to be acquired and the superior versatility

of such kind of modules.

The signals obtained from the four monitors are fed to the preamplifier (CANBERRA 2003BT) which gives time and energy signals as outputs. The energy signals obtained as output from the preamplifier are connected to the inputs of two ORTEC 855 dual fast shaping amplifiers. The typical amplitude of the signals often exceeds the range of the peak-sensitive Analog-to-Digital Converter (ADC) despite using the lowest possible gain. Therefore an appropriate attenuator (Quad Rotary Attenuator) is employed. Finally, the signal is stretched by an ORTEC 542 module, before it is processed by the ADC. The time signals are processed in a different way. First they are amplified with a fast amplifier (ORTEC 9309-4) and then sent to a Constant Fraction Discriminator (CFD) model PHILLIPS 715. The output signals of the CFD are sent to a gate generator (ORTEC GG8010) and then to a logical unit, where the four monitor signals are put in OR with the time signal of the silicon detector placed in the ionisation chamber.

A time signal is provided by each MCP. This signal is passed through a time pick-off pre-amplifier (PHILLIPS 6955) and fed into the CFD (PHILLIPS 715). The output signals of the CFDs are delayed and used as stop and/or start of the TAC module ORTEC-566. Three TAC modules are used to provide three time of flight signals TOF1, TOF2 and TOF3 respectively. Each TAC is started by the signal of the detector with lower rate, in order to prevent that the TAC receives signals not followed by a stop. So, the signals of the MCP, which are conveniently delayed, are employed to provide the stop for the two TACs which measure the time of flight between the first (second) MCP and the silicon detector, designated as TOF1 (TOF3). To measure the time of flight between the two MCPs (TOF2) another TAC is employed.

The silicon detector has an electronic chain similar to that of the monitors. After the pre-amplification, the energy signal is further amplified (CANBERRA 2024), sent to the linear gate and stretcher (ORTEC 542) and subsequently to the ADC. The time signal is fed to a fast amplifier and subsequently to a CFD. CFD gives three output signals out of which two output signals are used as start of TOF1 and TOF3, while the third one is sent to the gate generator (ORTEC GG8010). The output of this gate generator is sent in logical OR with monitors

and the output of the logic unit provides the trigger which enables the data acquisition. The ADC is used in its full dynamic range i.e. 4096 channels.

The energy signal provided by the ionization chamber passes through a pre-amplifier (ORTEC 2006E) and then is further amplified by a CANBERRA 2020 shaping amplifier. The output feeds the linear gate and stretcher to be finally processed by the ADC.

Chapter 5

Data analysis

5.1 Experimental procedure

The experiment was performed at the XTU Tandem in LNL for eight days. The experiment was designed to perform a detailed measurement of the ^{12}C+^{24}Mg fusion cross-section above and below the Coulomb barrier. The tandem accelerator provided ^{24}Mg beam with an average current of about 5 pnA. The thin ^{12}C target had a thickness of about 50 μg/cm^2 with isotopic enrichment of 99.99%. This high level of enrichment was used in order to minimize contribution from ^{13}C to the fusion yield.

The Coulomb barrier of the ^{12}C+^{24}Mg system is 34.5 MeV, as estimated using the Akyuz-Winther potential [8]. The energy range of the incident beam was chosen from 26-52 MeV in order to cover the values above, around and below the Coulomb barrier. However, the effective beam energy is less than the incident beam energy. This is due to the loss of the beam energy in the target.

The effective beam energy in the lab frame was calculated using the relation:

$$E_{lab} = E_{beam} - \frac{1}{2}\frac{dE}{dx}dx_t \tag{5.1}$$

where E_{beam} is the incident energy of the beam.

$\frac{dE}{dx}$ is the energy loss per unit length of the target.

dx_t is the thickness of the target.

The energy loss per unit length in the target was obtained using the software 'The Stopping and Range of Ions in Matter'(SRIM) [41]. SRIM is a group of programs which calculates the stopping and range of ions (up to 2 GeV/amu) into matter using a quantum mechanical treatment of ion-atom collisions. It is assumed that a moving atom is an ion and all target atoms are atoms.

The beam energy in the experiment was started from the highest value and gradually decreased till the lowest value. This was done in order to minimize hysteresis phenomena in the analyzing magnet which is placed at the exit of the accelerator. With every change in the energy beam, the beam was refocused on the target using a quartz. The change in energy was made with a gap of 0.5 MeV below 30 MeV in order not to miss out details in the deep sub-barrier region.

To obtain the fusion cross-section, direct detection of fusion evaporation residue technique was employed. The evaporation residues (ER) were separated from the beam and beam-like particles using the electrostatic deflector. The voltage applied to the electrodes of the electrostatic deflectors were modified for each energy value to give the maximum yield of the evaporation residues.

The particles that exit the electrostatic deflector are not only the evaporation residues. The ERs need to be further identified from the degraded beam. This identification was done using a double Time-of-Flight (TOF)-ΔE-Energy telescope composed of two micro-channel plate time detectors followed by the ionization chamber (IC) and by the silicon detector placed in the same gas (CH_4) volume of the IC. The IC provided the total energy loss signal ΔE. The silicon detector placed at the end of the detector telescope provided the residual energy of the ER and gave the start signal for the two TOF measured together with the micro channel plate (MCP) detectors. The silicon detector also provided the trigger for the data acquisition.

The ER are emitted at the forward angles. The measurements were done at an angle of 2^o for incident beam energy values from 52 MeV till 38 MeV. However, with the decrease in the value of the energy, the ER count decreases and at the same time more random coincidences come into the picture. To overcome this problem to some extent, the angle of measurement was increased. For energy values from 38 MeV till 27.5 MeV, the measurements were performed at 3^0. For

the subsequent energies till 26 MeV, the angle of measurement used was 4^0. So, in total, there were three angles of measurement viz. $2^o, 3^o$ and 4^o.

The beam has been monitored using four silicon detectors placed in the reaction chamber symmetrically around the beam direction. They are placed at a scattering angle of 16.1^o. The measurements from these monitors were used to normalize the fusion yields to the Rutherford scattering cross-section as the monitors detect the elastic scattered events.

An ER angular distribution measurement was performed in order to calculate the total fusion cross-section from the differential cross-section. The measurement was performed for the incident beam energy of 42 MeV for the angle range from -7^o to 7^o.

5.2 Analysis of $^{12}C + ^{24}Mg$ data

As mentioned in Chapter 4.2, the telescope provides three times of flight (TOF1, TOF2 and TOF3), a total energy loss ΔE and a residual energy E_{Si}. The correlation between these variables is used to identify the ER.

Fig. 5.1 shows the TOF3 vs E_{Si} for the measurement performed at incident beam energy of 37 MeV. The events enclosed within the polygon represent the ER and are clearly visible and distinguishable from the residual beam.

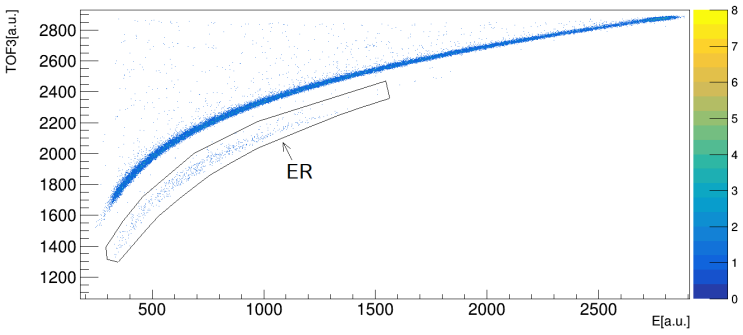

Figure 5.1: Time of flight TOF3 as a function of the residual energy E_{Si} at the beam energy of 37 MeV

As the energy drops below the barrier (34.5 MeV in our case), the ER counts

decrease significantly and it becomes difficult to distinguish the ER events from the background. This is due to the fact that in order to have significant ER counts at these energies, longer acquisition time is required. This, in turn, produces more random coincidences. Fig. 5.2 shows the TOF3 vs E_{Si} matrix at the beam energy of 31 MeV, which is the lowest measured energy where the ER events are still visually distinguishable.

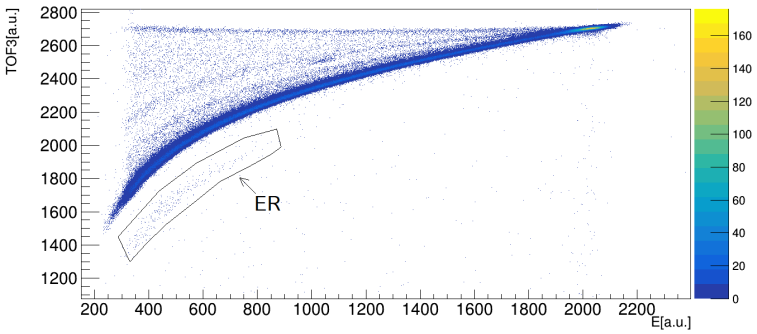

Figure 5.2: Time of flight TOF3 as a function of the residual energy E_{Si} at the beam energy of 31 MeV, which is the lowest energy where ER can be distinguished visually in the matrix.

For the subsequent measurements at lower energies, certain coincidences with the ER observed in other matrices were used in order to filter out the ER events from the background. The TOF1 vs ΔE matrix and the TOF1 vs E_{Si} matrix were used for this purpose. From the matrices TOF1 vs ΔE and TOF1 vs E_{Si}, events which best represent the ER events are selected using different polygons.

These selected events are used in coincidence with the events selected in the TOF3 vs E_{Si} matrix to get just the ER events. The polygon used in the matrix TOF3 vs E_{Si} is the same for the measurement at 31 MeV of Fig. 5.2.

In Fig. 5.3 (upper left panel) the TOF3 vs E_{Si} matrix of the measurement performed at 30 MeV is shown. It can be noticed that it is unclear whether the polygon contains just ER events or a big proportion of background too. By applying a coincidence with the ER in the TOF1 vs E_{Si} and TOF1 vs ΔE matrices (top right and bottom left panels, respectively), the ER can be better identified in the TOF3 vs E_{Si} matrix (bottom right panel) where most of the backgrounds

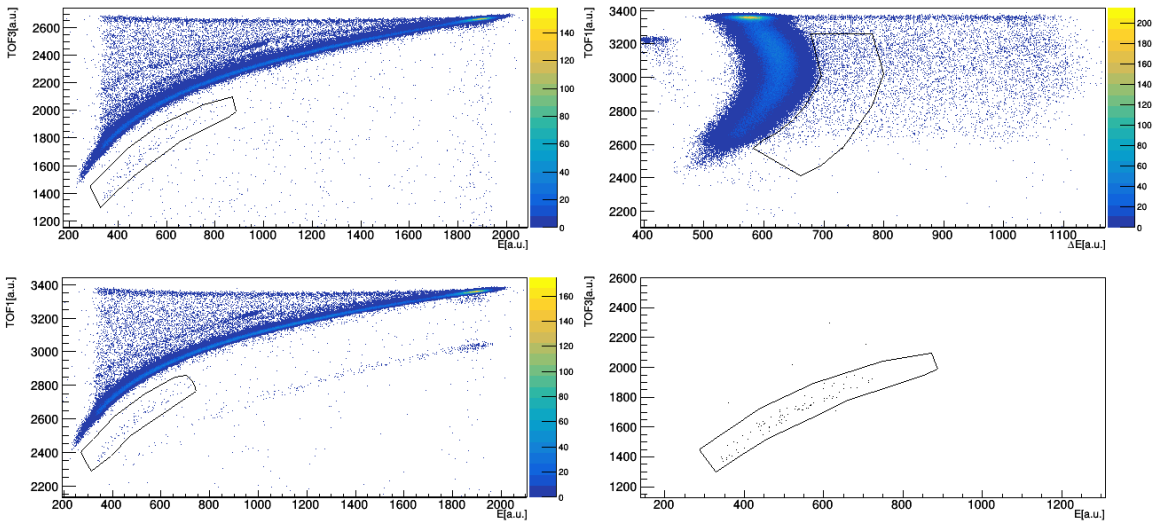

Figure 5.3: (Upper left panel) Time of flight TOF3 as a function of the residual energy E_{Si} at the beam energy of 30 MeV. The same matrix is shown in the bottom right panel, after that the ER identified both in the TOF1 vs ΔE (upper right panel) and TOF1 vs E_{Si} (bottom left panel) matrices have been selected.

and the residual beam have been removed. This method was applied to determine the number of ER events at sub-barrier energies.

The four silicon detectors in the reaction chamber were used to detect the scattered beam nuclei at an angle of 16.1^o, with respect to the beam direction. Fig. 5.4 and Fig. 5.5 show the 1D spectra provided by the four monitors at two representative energies, where the peaks indicate the elastic scattered nuclei measured at energies above and below the Coulomb barrier. It can be observed that the peaks shift with the change in energy and hence the number of events was estimated by changing the interval of channel for each energy value.

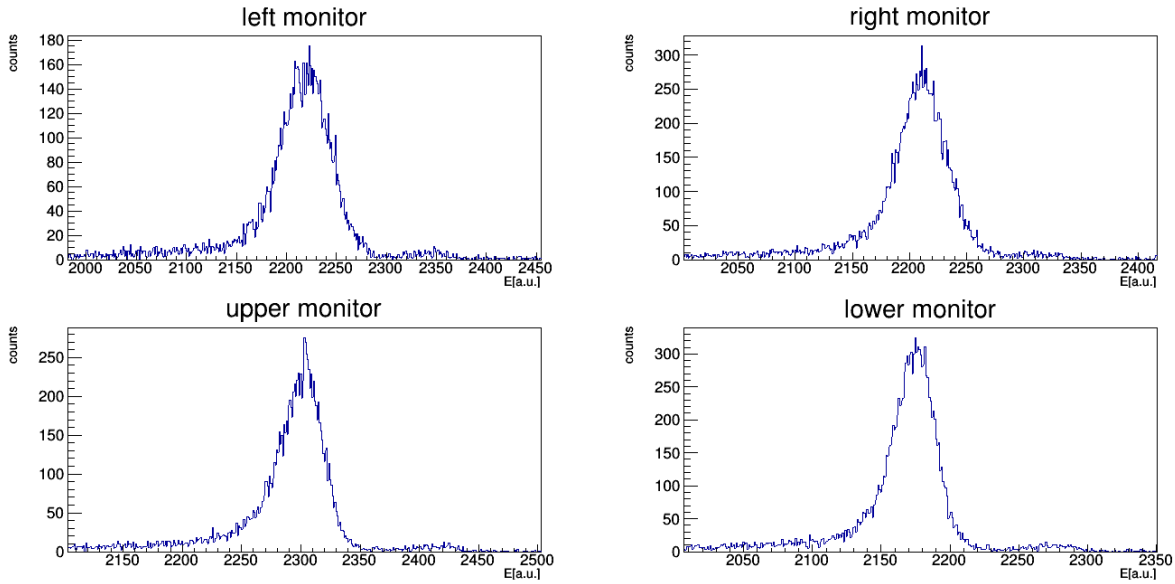

Figure 5.4: Energy spectra of the four monitors at the beam energy of 37 MeV

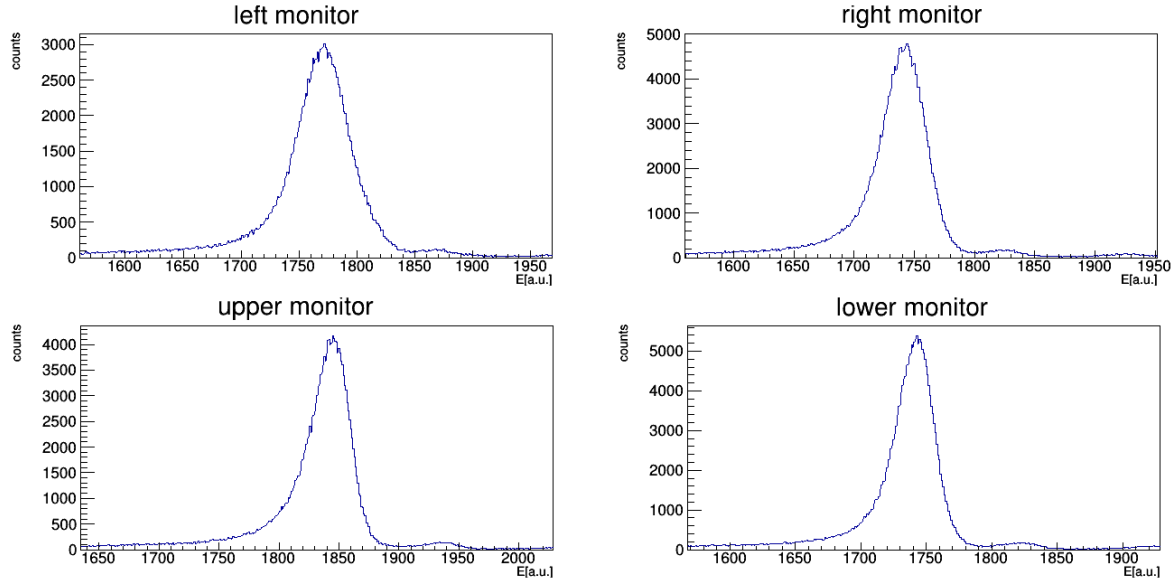

Figure 5.5: Energy spectra of the four monitors at the beam energy of 30 MeV

After measuring the ER and monitor counts (N^{ER} and N^{Mon} respectively), the differential fusion cross section $\frac{d\sigma}{d\Omega}(E)$ for each energy was estimated using the following equation:

$$\frac{d\sigma}{d\Omega}(E) = \frac{N^{ER}}{N^{Mon}} \frac{\Delta\Omega^{Mon}}{\Delta\Omega^{geom}_{fus}} \frac{d\sigma_R}{d\Omega}(E) \frac{1}{T \times t \times t_{IC}} \tag{5.2}$$

where

$\Delta\Omega^{Mon}$ is the solid angle of the 4 monitors = 0.167 msr ±1%

$\Delta\Omega^{geom}_{fus}$ is the geometrical solid angle of the Si monitor = 0.050 msr ±1%

T is the estimated transmission of the electrostatic deflector = 0.82 ±3.6%

t is the transparency of the grids of the 2 MCP detectors = 0.726 ±0.5%

t_{IC} is the total transparency of the IC entrance window and electrodes = 0.533±1%

The events detected in the 4 silicon monitors are elastically scattered events. Therefore, the differential cross-sections need to be normalized with respect to the Rutherford cross-section, which accounts for the elastically scattered events. The Rutherford cross-section $\frac{d\sigma_R}{d\Omega}(E)$ was calculated using the expression:

$$\frac{d\sigma_R}{d\Omega}(E) = \left(\frac{Z_p Z_t e^2}{16\pi\epsilon_o E_{lab}}\right)^2 \left[\frac{1}{sin^4(\theta_{lab}/2)} - 2\left(\frac{M_p}{M_t}\right)^2 + \left(\frac{M_p}{M_t}\right)^4\right] \; mb/sr \tag{5.3}$$

where

Z_p and Z_t are the atomic number of the projectile and the target respectively.

M_p and M_t are the mass number of the projectile and the target respectively.

E_{lab} is the effective beam energy in the lab frame.

θ_{lab} is the angle where the monitors are placed with respect to the beam direction = 16.1^o.

Using Eq. (5.2) and Eq. (5.3), the differential cross-section was calculated for each measured energy.

The calculated differential cross-sections have uncertainties due to statistical errors and systematic errors.

As the count of the particles follow a Poisson distribution, the statistical errors in the measurements of N^{ER} and N^{Mon} are simply calculated as,

$$\delta_i = \sqrt{x_i}$$

Therefore, the contribution of statistical error in the calculation of the differential cross-section is given by

$$\begin{aligned}\delta(\frac{d\sigma}{d\Omega})_{stat} &= \frac{d\sigma}{d\Omega}\sqrt{\Big(\frac{\delta N_{ER}}{N^{ER}}\Big)^2 + \Big(\frac{\delta N_{Mon}}{N^{Mon}}\Big)^2} \\ &= \frac{d\sigma}{d\Omega}\sqrt{\Big(\frac{\sqrt{N^{ER}}}{N^{ER}}\Big)^2 + \Big(\frac{\sqrt{N^{Mon}}}{N^{Mon}}\Big)^2} \\ &= \frac{d\sigma}{d\Omega}\sqrt{\Big(\frac{1}{N^{ER}}\Big) + \Big(\frac{1}{N^{Mon}}\Big)}\end{aligned}$$

The systematic error in the calculation of the differential cross-section is determined by the measurement of the solid angles of the monitors and the Si detector and the measurements of T, t and t_{IC}. The uncertainty of the differential cross-section due to systematic error is given by

$$\begin{aligned}\delta(\frac{d\sigma}{d\Omega})_{sys} &= \frac{d\sigma}{d\Omega}\sqrt{\Big(\frac{\delta(\Delta\Omega^{Mon})}{\Delta\Omega^{Mon}}\Big)^2 + \Big(\frac{\delta(\Delta\Omega^{geom}_{fus})}{\Delta\Omega^{geom}_{fus}}\Big)^2 + \Big(\frac{\delta T}{T}\Big)^2 + \Big(\frac{\delta t}{t}\Big)^2 + \Big(\frac{\delta t_{IC}}{t_{IC}}\Big)^2} \\ &= \frac{d\sigma}{d\Omega}\sqrt{\Big(1\%\Big)^2 + \Big(1\%\Big)^2 + \Big(3.6\%\Big)^2 + \Big(0.5\%\Big)^2 + \Big(1\%\Big)^2} \\ &= \frac{d\sigma}{d\Omega} \times 4.3\%\end{aligned}$$

The main contribution of the systematical error is from T, the estimated transmission of the electrostatic deflector.

The total fusion cross-section is calculated by integrating the differential cross section over all the solid angle:

$$\begin{aligned}\sigma_{tot} &= \int_0^{4\pi} \frac{d\sigma}{d\Omega} d\Omega \\ &= 2\pi \int_0^{\pi} \frac{d\sigma}{d\theta} sin\theta d\theta\end{aligned} \tag{5.4}$$

In order to perform the above integration, an angular distribution measurement was performed.

5.3 Angular distribution

The angular distribution was performed at the effective beam energy of 41.67 MeV, which is above the Coulomb barrier of the system. The differential fusion cross-sections were measured for the angles -7^o, -6^o, -5^o, -4^o, -3^o, 2^o, 4^o, 5^o, 6^o, 7^o and 8^o. The experimental values are reported in Table. A.1.

The width and shape of the angular distribution might vary with energy. To check if there is change in width and shape of the distribution, the Monte-carlo code PACE4 was used. PACE4 is a program, in the LISE^{++} framework, that allows to calculate fusion cross-section below the Coulomb barrier using quantum mechanical approach [42]. Using PACE4, the theoretical differential cross-sections were calculated at 41.67 MeV. The theoretical values are different from the experimental values. And so these theoretical values were normalised with respect to the experimental values. The two angular distributions, theoretical and experimental, at 41.67 MeV are compared in Fig. 5.6, where a gaussian fit was performed separately for the two distributions.

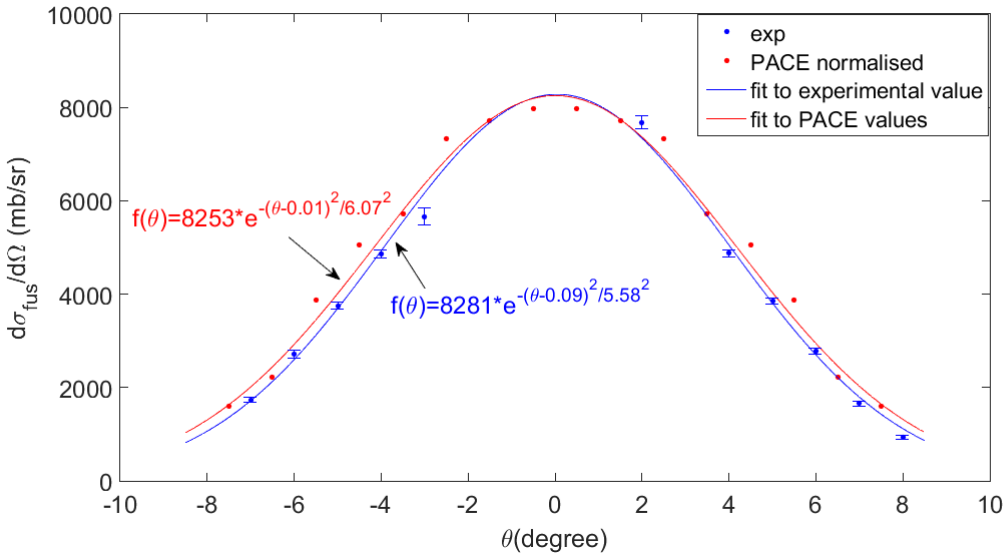

Figure 5.6: Experimental (blue dots) and PACE4 (red dots) angular distribution at the effective beam energy of 41.67 MeV. The gaussian fit of the experimental data (blue line) and of the PACE4 calculations (red line) are shown.

Using Eq. (5.4), the gaussian function obtained from the fit of PACE4 values was integrated over the whole solid angle to obtain the total fusion cross-section at 41.67 MeV. The obtained total fusion cross-sections were then divided by the differential fusion cross-section, estimated with PACE4 for an energy value at a particular angle θ, in order to obtain the integration factor (K(θ)).

For instance, the value of K at 2^o and at the effective beam energy of 41.67 MeV is calculated as

$$K(2^o, 41.67MeV) = \frac{(\sigma_{tot}^{PACE})_{41.67MeV}}{\frac{d\sigma}{d\Omega}^{PACE}(2^o)_{41.67MeV}} = 0.039 \tag{5.5}$$

Few energy values were chosen to calculate the integration factors in order to check the consistency of the integration factor. The choice of the energy values for which the PACE4 calculations were made depends on the values of energies in comparison with the Coulomb barrier which is 34.5 MeV in this case. Two energy values well above the Coulomb barrier viz. 41.67 and 40.67 MeV were chosen. Two energy values around the Coulomb barrier viz. 36.66 and 31.65 MeV were chosen and finally, two energy values well below the Coulomb barrier viz. 27.13 and 25.63 MeV were chosen. All the theoretical differential cross-section values obtained for these energies were normalised with the factor obtained in the case of 41.67 MeV.

Gaussian fits were performed for all the angular distributions estimated with PACE4. The total fusion cross sections at the energies of 40.67, 36.66, 31.65, 27.13 and 25.62 MeV were then estimated by integrating over all the solid angle.

The integration factors at the angle of 2^o, 3^o and 4^o were then calculated using Eq. (5.5) for each energy. The values obtained are listed in Table 5.1.

Energy(MeV)	K(2^o)	K(3^o)	K(4^o)
41.67	0.039	0.044	0.054
40.67	0.037	0.042	0.052
36.66	0.041	0.046	0.055
31.65	0.042	0.047	0.056
27.13	0.040	0.046	0.058
25.63	0.042	0.047	0.056
Mean	0.04	0.045	0.055

Table 5.1: The integration factors K(2^o), K(3^o) and K(4^o) estimated with PACE4 calculations

The mean values K(2^o)= 0.040 ± 0.001, K(3^o)= 0.045 ± 0.001 and K(4^o)= 0.055 ± 0.002 with 95% confidence level were used in the further calculations.

5.4 Total fusion cross sections and excitation function

The integration factors K(2^o), K(3^o) and K(4^o) extracted in the previous subsection, have been used to estimate the total cross-section for each energy. From Eq. (5.5), it is clear that the experimental total cross-section can be obtained by multiplying the experimental differential cross-section with the corresponding K-values.

$$\sigma_{tot}^{exp}(E) = K(\theta)\frac{d\sigma^{exp}}{d\Omega}(\theta, E) \tag{5.6}$$

The uncertainty in the calculation of the total fusion cross-section is a total contribution of the uncertainty of $K(\theta)$ and the calculation of the differential cross-section, which is discussed before.

$$\left[\frac{\delta\left(\sigma_{tot}^{exp}\right)}{\sigma_{tot}^{exp}}\right]^2 = \left[\frac{\delta K(\theta)}{K(\theta)}\right]^2 + \left[\frac{\delta\left(\frac{d\sigma^{exp}}{d\Omega}\right)}{\frac{d\sigma^{exp}}{d\Omega}}\right]^2 \tag{5.7}$$

A weighted mean cross section was estimated for the measurements performed at the same energy. The weighted mean of the total cross-sections and the errors were obtained using the relation:

$$\bar{x} = \frac{\sum \frac{x_i}{\delta_i^2}}{\sum \frac{1}{\delta_i^2}} \tag{5.8}$$

$$\bar{\delta} = \frac{1}{\sum \frac{1}{\delta_i^2}} \tag{5.9}$$

where x_i represents the measured quantity (cross-section) and δ_i is the associated error.

The fusion cross sections and their statistical errors are reported in Table A.2 of the Appendix. The excitation function of the system, which is the plot of the total cross-section as a function of the energy in the center of mass frame (E_{cm}) is shown in Fig. 5.7.

The E_{cm} was obtained as:

$$E_{cm} = \frac{\mu}{m_p} E_{lab} = \frac{m_t}{m_t + m_p} E_{lab} = \frac{1}{3} E_{lab} \tag{5.10}$$

where m_p is the mass of the projectile ^{24}Mg and m_t is the mass of the target ^{12}C.

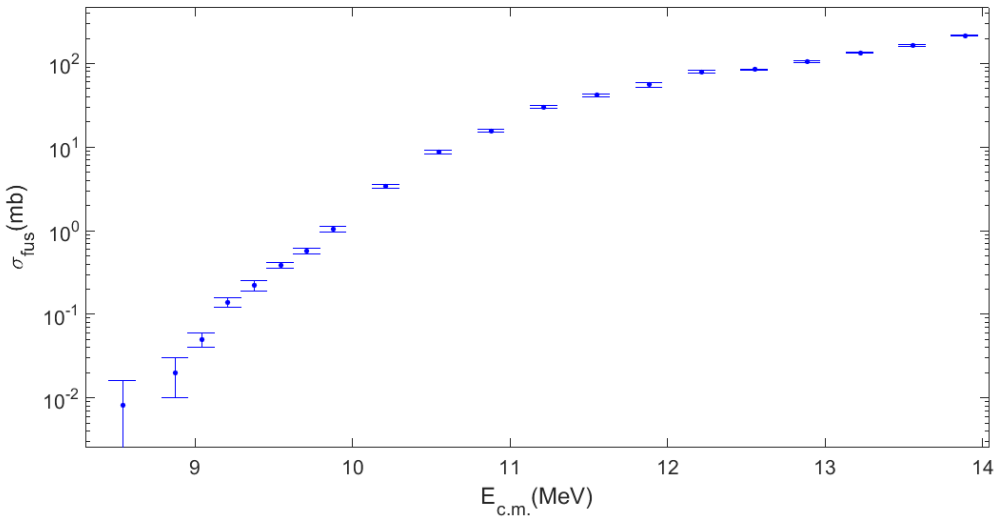

Figure 5.7: Experimental excitation function of ^{24}Mg+^{12}C system

5.5 Astrophysical S-factor and logarithmic slope

The astrophysical S-factor S(E) is a re-scaled variant of the total cross-section σ(E) that accounts for the Coulomb repulsion between the charged reactants. It is a very important quantity in heavy ion fusion at sub-barrier energy. The trend of the S-factor provides information on the hindrance effect.

The S-factor is calculated as:

$$S(E) = E\sigma(E)e^{2\pi(\eta-\eta_o)} \tag{5.11}$$

where

E is the energy in center of mass frame.

η=0.157$\frac{Z_p Z_t}{\sqrt{E/\mu}}$ and η_o is a convenient scaling factor.

The values of astrophysical S-factor with their statistical errors for different energies are reported in Table A.3.

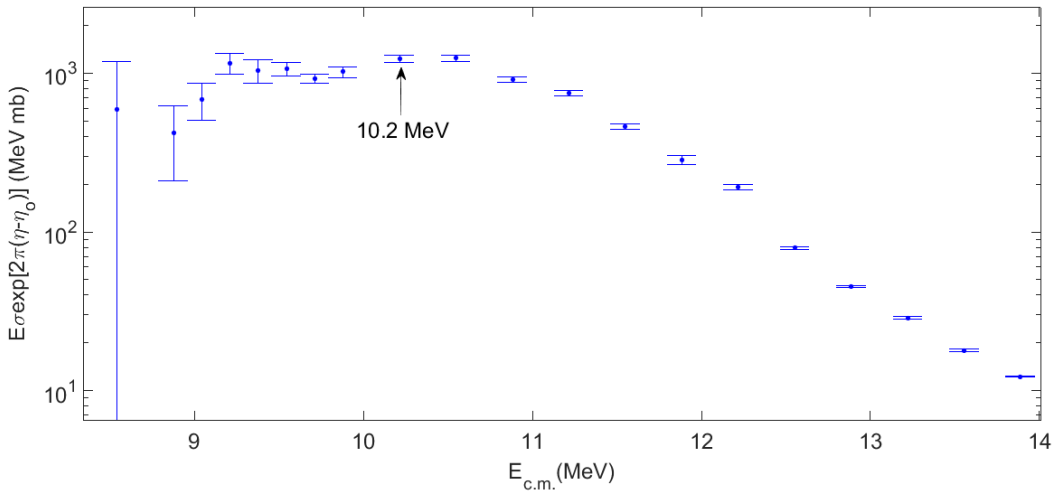

Figure 5.8: S-factor of ^{24}Mg+^{12}C system

As can be observed from Fig. 5.8, the S-factor displays a maximum around the energy E_{cm} = 10.2 MeV. This maximum can be related to the presence of hindrance phenomena.

To check the validity of this result, another quantity called the logarithmic slope was calculated. Logarithmic slope L(E) is given by the relation:

$$L(E) = \frac{d}{dE}[ln(E\sigma)] \tag{5.12}$$

S(E) develops a maximum when $\frac{dS}{dE}$=0 i.e. when L(E)= $\frac{\pi\eta}{E}$= L_{CS}. The corresponding energy E=E_S is generally considered the threshold energy of hindrance effect [33]. It means that if plots of L(E) and L_{CS} as a function of energy are made, they must meet at an energy value equal to E_S which is around 10.2 MeV in this case.

Two methods were employed to calculate the logarithmic slope of the system. In the first method, alternate data points were considered and the logarithmic slope was calculated directly from the experimental data using the 'three-point formula'.

$$L(E_i) = \frac{ln(E_{i+1}\sigma_{i+1}) - ln(E_{i-1}\sigma_{i-1})}{E_{i+1} - E_{i-1}} \tag{5.13}$$

Values of the logarithmic slope calculated using Eq. (5.13) and their errors are reported in Table. A.4.

In the second method, a fit was performed on the plot of $ln(E\sigma)$ as a function of energy E_{cm} as shown in Fig. 5.9.

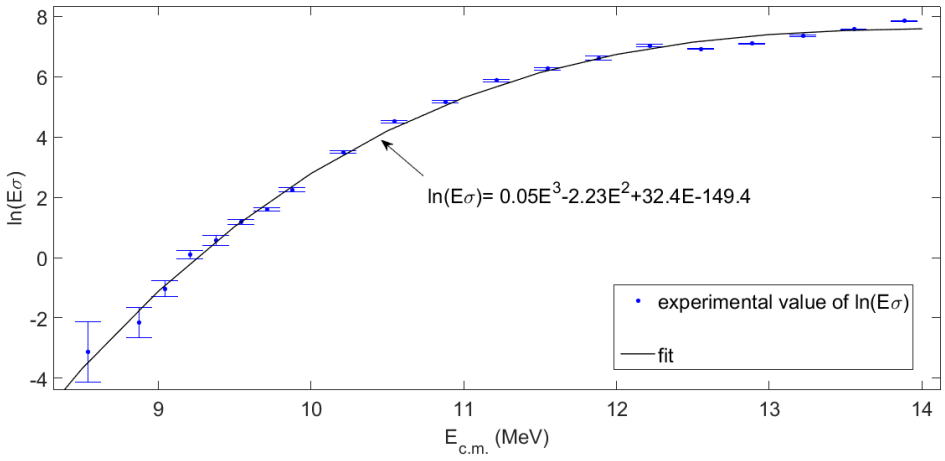

Figure 5.9: $ln(E\sigma)$ as a function of energy. The blue dots represent the experimental values and the brown line represents the fit.

The derivative of the fit function was made with respect to energy to obtain the logarithmic slope L(E).

$$\begin{aligned} L(E)^{fit} &= \frac{d}{dE}[ln(E\sigma)]^{fit} \\ &= \frac{d}{dE}[0.05E^3 - 2.23E^2 + 32.4E - 149.4] \\ &= 0.15E^2 - 4.46E + 32.4 \end{aligned} \tag{5.14}$$

This calculated expression of L(E) from the fit of $ln(E\sigma)$ was plotted along with the values of L(E) calculated from the first method and L_{CS} to extract the value of E_S as shown in Fig. 5.10.

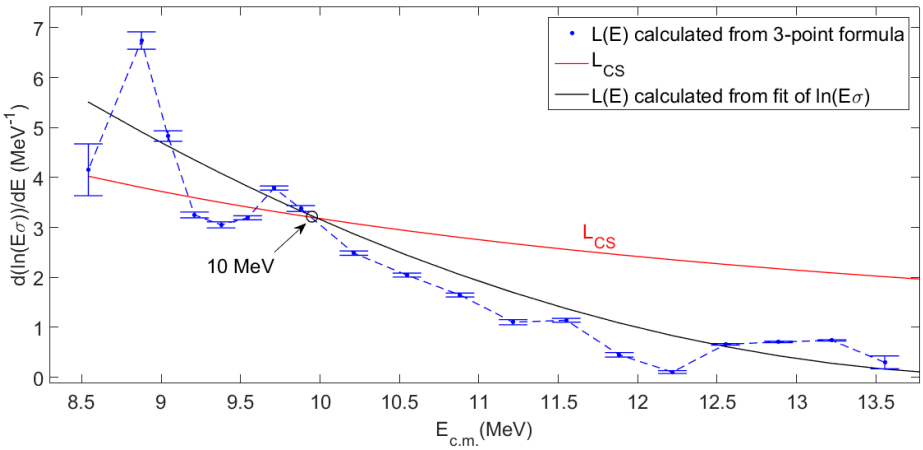

Figure 5.10: Logarithmic slope of ^{24}Mg+^{12}C system

It is observed that L(E) and L_{CS} meet at the energy value of 10 MeV which is very close to 10.2 MeV where the maximum of the S-factor was observed. The result can be considered consistent when statistical and systematic uncertainties are taken into consideration.

The presence of hindrance effect can be confirmed by comparison of experimental cross-sections with the coupled-channel calculations.

5.6 Comparison with CC calculations

CCFULL is a FORTRAN 77 program that calculates fusion cross sections under the influence of couplings between the relative motion and several nuclear collective motions [7]. The comparison of the experimental cross-sections with the CCFULL calculation provides information on hindrance effect if it is observed at the energies for which the experiment was performed.

Vibrational coupling to the quadrupole state 2^+ of ^{24}Mg at 1.39 MeV with β_2=0.61 is considered. The nominal Coulomb barrier of ^{12}C+^{24}Mg system at center of mass frame is 11.5 MeV. However, the CCFULL calculation made at this value of Coulomb barrier does not reproduce the experimental data as can be seen in Fig. 5.11. This is due to the shift in the Coulomb barrier, which is caused by coupling to higher excited states.

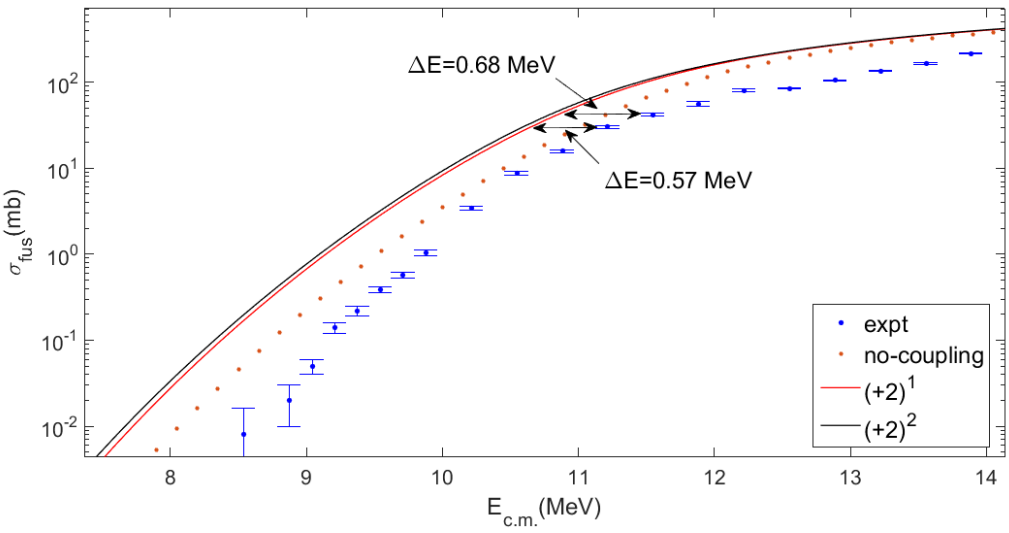

Figure 5.11: CCFULL calculation made at calculated Coulomb barrier of 11.5 MeV. The one phonon coupling to the first excited state of Mg is represented in red and the case for two phonons coupling in black. The brown dots represent the case for no coupling. The shifts in effective Coulomb barriers for the experimental values around 11.5 MeV are indicated.

This shift in the value of Coulomb barrier needs to be incorporated in the

CCFULL calculation. Values of the shift in Coulomb barrier were estimated for two experimental points around 11.5 MeV as shown in Fig. 5.11. The values were found to be 0.57 MeV and 0.68 MeV.

If V_b' represents the new Coulomb barrier, it should lie in the range

$$V_b + 0.57 \leq V_b' \leq V_b + 0.68 \ \ MeV$$
$$\Rightarrow 12.07 \leq V_b' \leq 12.18 \ \ MeV$$

The best value of V_b' that best fits the experimental data was found with a few trials within the defined range. The CCFULL calculation, finally, has been made with an effective Coulomb barrier of 12.13 MeV.

5.6.1 Evidence of the fusion hindrance phenomenon

The parameters of the Wood-Saxon potential used in the CCFULL calculation corresponding to the shifted barrier at 12.13 MeV is shown in Table. 5.2.

V_o(MeV)	r_o(fm)	a_o(fm)
43.37	1.09	0.60

Table 5.2: Well depth V_o, radius r_o and diffuseness a_o of the Wood-Saxon potential

Comparison of the experimental cross-sections with relevant calculations from CCFULL program is shown in Fig. 5.12. Experimental data points from two other experiments [36, 37] performed at higher energies were also included to check the validity of the CCFULL calculation as the data from the current experiment is observed to have some fluctuations at higher energies. The CCFULL calculation is in accordance with the experimental data at higher energies which means that the calculation is valid.

As can be observed in Fig. 5.12, the experimental cross-sections start to drop down compared to the CCFULL calculation at an energy value around 10.2 MeV. This drop in the fusion cross-sections at the sub-barrier energies is the evidence of fusion hindrance phenomenon. The S-factor was also observed to have a maximum

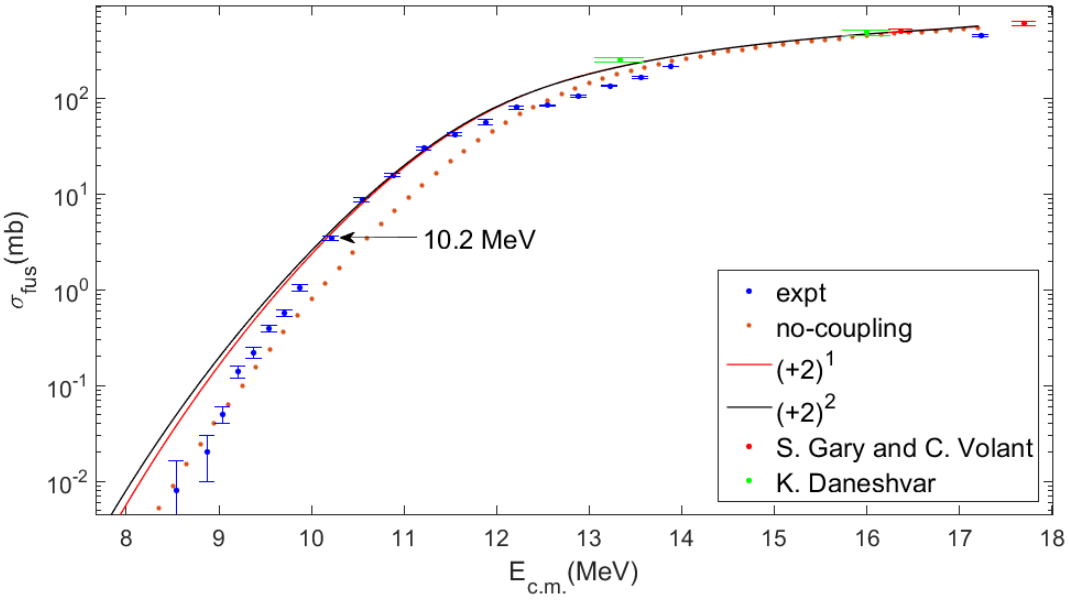

Figure 5.12: Comparison of experimental fusion cross-sections to the CCFULL calculations. The one phonon coupling to the first excited state of Mg is represented in red and the case for two phonons coupling in black. The brown dots represent the case for no coupling.

at around 10.2 MeV. This agreement from two different approaches can concretize the observation of hindrance effect in the ^{12}C+^{24}Mg system.

The obtained energy value of the threshold of hindrance is in good agreement with the emperical estimate by C.L. Jiang et al. [33]

Chapter 6

Systematic trends for heavy and light cases

6.1 Behavior of near-by systems: ^{12}C+^{30}Si , ^{24}Mg+^{30}Si

The result obtained for ^{12}C+^{24}Mg is in close agreement with the previous experiments performed on near-by systems ^{12}C+^{30}Si and ^{24}Mg+^{30}Si. All the three systems can provide guideline in extrapolating the behavior to the systems of astrophysical importance. The three systems have positive fusion Q-values.

System	Q-value (MeV)
^{12}C+^{24}Mg	+16.3
^{12}C+^{30}Si	+14.11
^{24}Mg+^{30}Si	+17.89

Table 6.1: Q-values of the systems

^{12}C+^{30}Si system

Fusion cross-sections measurement of the ^{12}C+^{30}Si was performed to study the hindrance at deep sub-barrier energies [6]. The Coulomb barrier of the system at the center of mass frame is around 13.1 MeV. The results of the experiment are briefly discussed.

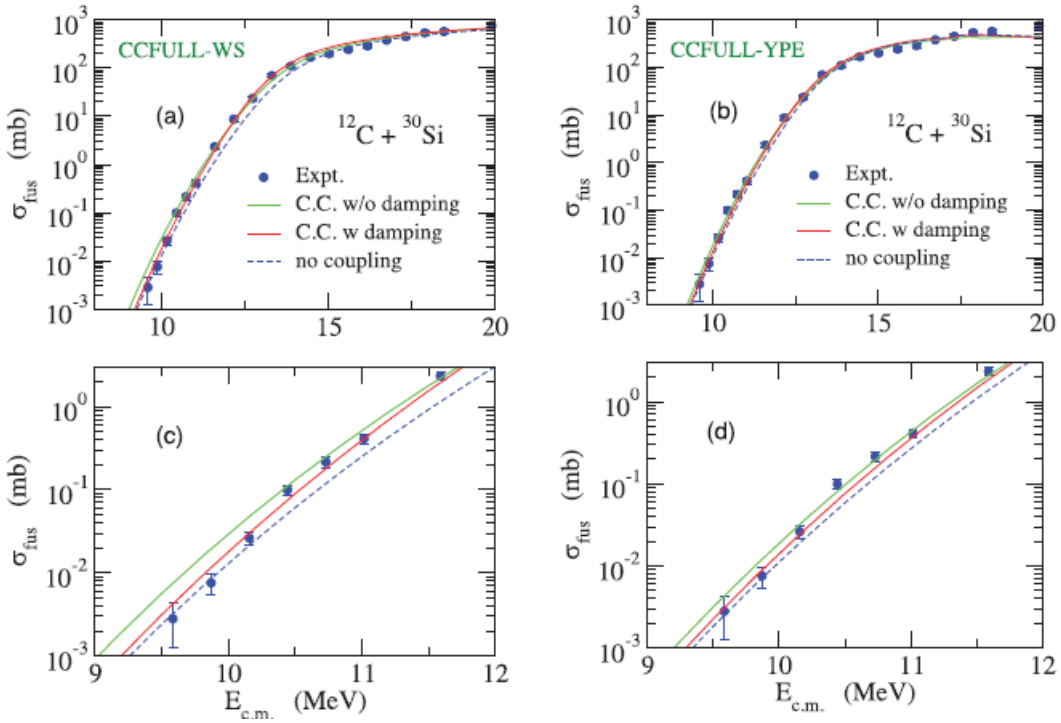

Figure 6.1: Experimental fusion cross-sections compared to CC calculations employing the WS (a) and (c), and the YPE (b) and (d) potentials, with and without damping of coupling strengths [6]. Expanded views of the low energy are shown in (c) and (d).

The CC calculations used to compared with the experimental fusion cross-section were made using two different potentials: the Wood-Saxon (WS) potential and the Yukawa-plus-exponential (YPE) potential. As observed from Fig. 6.1, there is a drop in the fusion cross-section compared to the standard CC calculation at energy around 10.5 MeV, which is well below the Coulomb barrier. This shows the presence of hindrance effect in the deep sub-barrier energies.

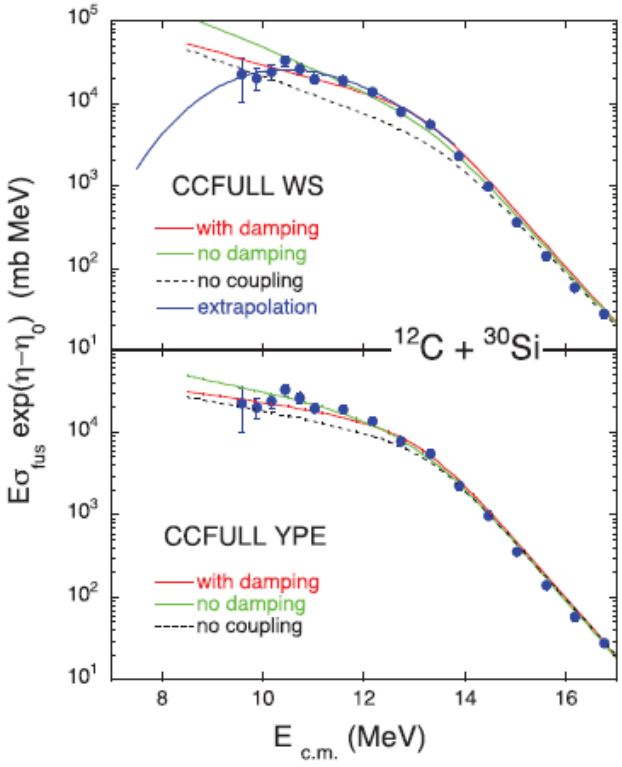

Figure 6.2: Astrophysical S-factor for the $^{12}C+^{30}Si$ in comparison with the CC calculations made with WS and the YPE potential [6]. A maximum tends to develop around 10.5 MeV.

The presence of the hindrance effect is also reflected on the astrophysical S-factor of the system where a maximum is observed around 10.5 MeV as shown in Fig. 6.2. The threshold of hindrance was found to be in agreement with the phenomenological estimate by C.L. Jiang et al. [33].

^{24}Mg+^{30}Si system

Fusion cross-sections measurement was also performed for the ^{24}Mg+^{30}Si system [43] for the study of hindrance at deep sub-barrier energies. The Coulomb barrier of the system at the center of mass frame is around 24.7 MeV. The results of this experiment are also briefly discussed.

As can be seen from Fig. 6.3, the standard CC calculation with the Woods-Saxon potential provides an excellent estimate of the fusion cross-sections above the Coulomb barrier. However at lower energies, it overpredicts the experimental data, which gives strong evidence of fusion hindrance.

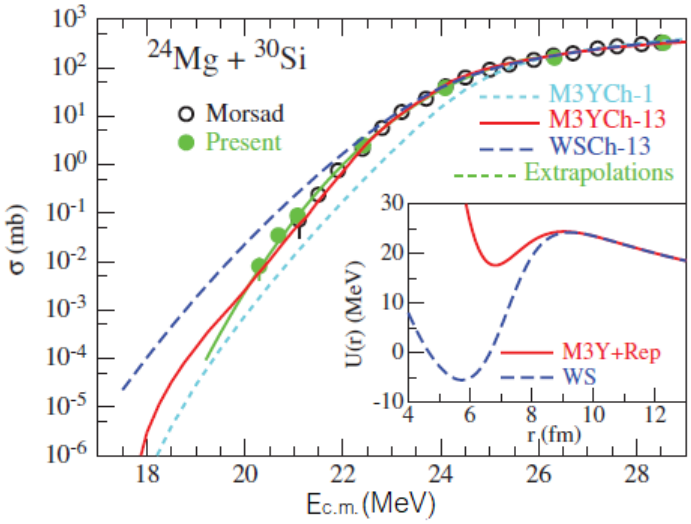

Figure 6.3: Experimental cross-sections (green dots) [43] and previous results by Morsad et al. (black open circles) [44]. CC calculations with the WS potential and the M3Y potential [30] are indicated. Ch-X indicates the number of channels considered [43].

The presence of hindrance is well evident in the astrophysical S-factor of the system as shown in Fig. 6.4. A clear maximum was observed at an energy value of 20.8 MeV. The obtained value of the threshold of hindrance also agrees with the phenomenological estimate by C. L. Jiang et al. [33].

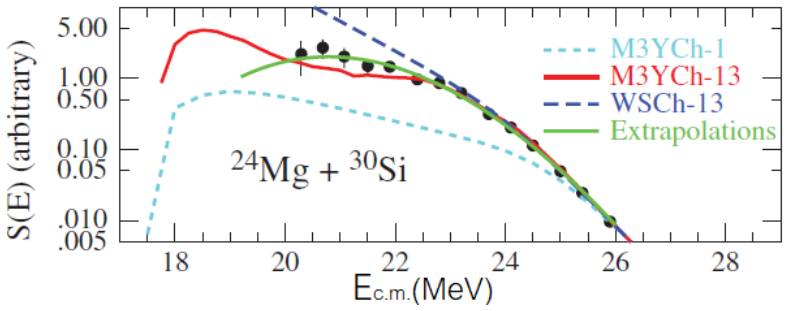

Figure 6.4: S(E) of the ^{24}Mg+^{30}Si system [43]. CC calculations with WS and the M3Y potential [30] are indicated. Ch-X indicates the number of channels considered [43].

It has been clearly observed that a maximum of the S-factor is developed in the case of systems with positive Q-values. By extrapolation to lighter systems, one can expect similar reduction in the cross-sections for other systems with positive Q-values which are of astrophysical importance.

6.2 Extrapolation to lighter systems and systematics

A general parametrization was proposed to describe the excitation functions for a wide range of light systems at low energies [33]. Systematics of heavy ion fusion hindrance for systems with positive fusion Q-values are briefly discussed below.

The two representations: S-factor S(E) and the logarithmic slope L(E) of fusion cross-section have been employed for this purpose. S(E) eliminates the strong energy dependence originating from the tunneling through the Coulomb barrier. On the other hand, L(E) eliminates normalization and efficiency errors in the experimental data. Although both representations are not clearly independent, the parametrizations have been used.

The extrapolation was suggested for the logarithmic slope [45] as

$$L(E) = A_0 + \frac{B_0}{E^{N_p}} \ \text{MeV}^{-1} \tag{6.1}$$

where A_0 and B_0 are the fit parameters and the exponential N_p is somewhat arbitrary but generally assumed to be 1.5.

The threshold energy of hindrance is denoted by E_S and the value of L(E) at this energy value is denoted by L_S. They are expressed as [33]:

$$E_S = \left(\frac{0.495\zeta - B_0}{A_0}\right)^{2/3} \ \text{MeV} \tag{6.2}$$

$$L_S = \frac{0.495\zeta A_0}{0.495\zeta - B_0}^{2/3} \ \text{MeV}^{-1} \tag{6.3}$$

where ζ is the entrance channel parameter defined in Eq. (3.1).

The corresponding extrapolated cross-section $\sigma(E)$ can then be expressed as [45]

$$\sigma(E) = \sigma_S \frac{E_S}{E} e^{[A_0(E-E_S)-B_0\frac{1}{E_S^{N_P-1}(N_P-1)}((\frac{E_S}{E})^{N_P-1}-1)]} \tag{6.4}$$

where σ_S is the fusion cross-section at threshold.

As can be clearly seen from Fig. 6.5, the black solid dots are well described by the empirical functions E_S^{emp} and L_S^{emp} which were developed as [33]:

$$L_S^{emp} = 2.33 + 580/\zeta \ \text{MeV}^{-1} \tag{6.5}$$

$$E_S^{emp} = \left[0.495\zeta/L_S^{emp}(\zeta)\right]^{2/3} \ \text{MeV} \tag{6.6}$$

The empirical equations of A_0^{emp} and B_0^{emp} were also developed as shown in Fig. 6.6 and are expressed as [33]:

$$A_0^{emp} = -10/\zeta - 1.13 - 0.0065\zeta \ \text{MeV}^{-1} \tag{6.7}$$

$$B_0^{emp} = 0.495\zeta\left[1 - A_0^{emp}(\zeta)/L_S^{emp}(\zeta)\right] \ \text{MeV}^{1/2} \tag{6.8}$$

Using equations (6.5), (6.6), (6.7) and (6.8), one can predict the shape of the excitation function at very low energies, including the contribution from the fusion hindrance [33].

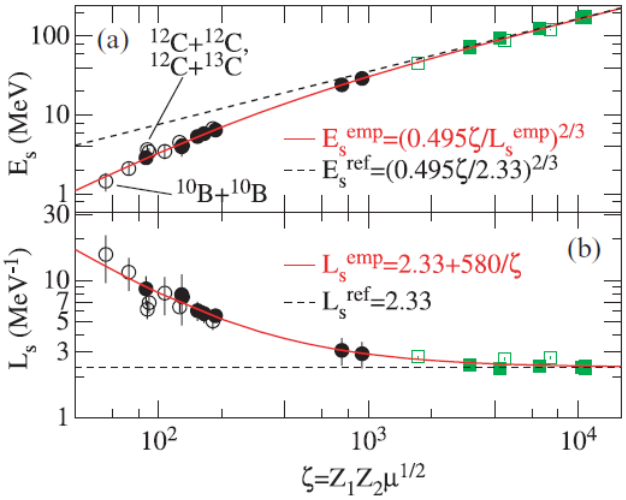

Figure 6.5: Plot of E_S (a) and L_S (b) versus ζ [33]. The systems with positive or negative Q-values are indicated by black circles and green circles, respectively. The black solid dots represent the systems analyzed in Ref. [33].

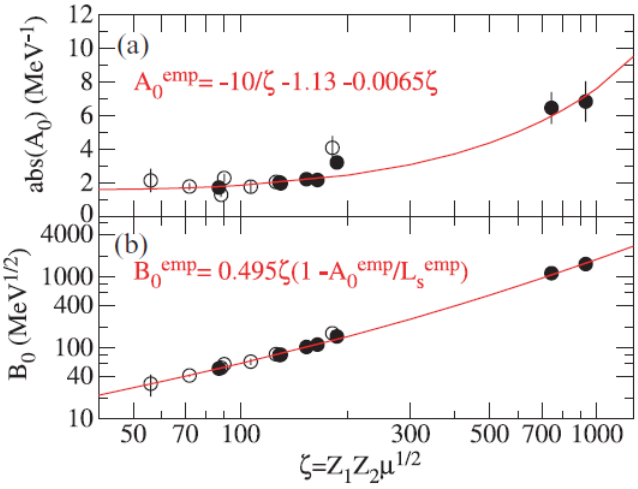

Figure 6.6: Plot of A_0 (a) and B_0 (b) against ζ for lighter heavy ions. Only systems with positive Q-values are included. The black solid dots represent the systems analyzed in Ref. [33].

A detailed plot of the E_S^{emp} as a function of the entrance channel parameter ζ with the experimentally obtained values of E_S for different systems are shown in Fig. 6.7.

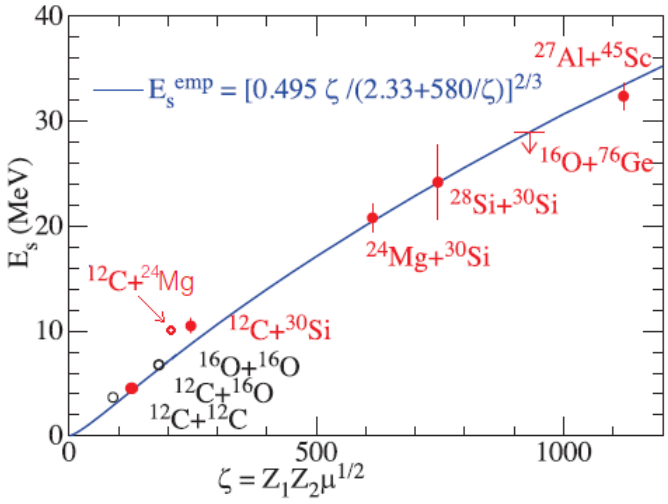

Figure 6.7: Systematics of E_S in several light- and medium-light mass systems [6]. Blue line represents the empirical calculation E_S^{emp} and red dots represent the experimental values of E_S for different systems

As can be observed from the figure, the experimental values of the threshold energy of hindrance E_S are in good agreement with the empirical calculation E_S^{emp}.

Chapter 7

Summary and Conclusions

This thesis discussed the theoretical approach to heavy-ion fusion and the experimental study of heavy-ion fusion of $^{12}C+^{24}Mg$ in inverse kinematics. The excitation function of $^{12}C+^{24}Mg$ system above and below the Coulomb barrier has been measured. The purpose of the experiment was to study the effect of coupling in the fusion cross-section and most importantly the fusion hindrance in the deep sub-barrier energies. The events were registered in an experiment performed at LNL using the PISOLO set-up. The fusion excitation function of the system was measured down to 10 μb. A standard CCFULL calculation was made which well described the excitation function above the Coulomb barrier. However, a drop in the excitation function compared to the CCFULL calculation was observed at around 10.2 MeV which indicated the presence of hindrance at deep sub-barrier energies. The threshold of hindrance is in agreement with the phenomenological estimate [33]. This is one more case close to the systems of astrophysical importance, which shows hindrance effect.

Appendix A

Appendix: Tables of experimental data

A.1 Angular distribution

The angular distribution has been measured at an effective beam energy of 41.67 MeV. The differential cross-sections are reported in Table A.1.

θ(deg)	d$\sigma_{fus}/d\Omega$(mb/sr)
-7	1737±49
-6	2711±86
-5	3754±77
-4	4864±83
-3	5663±179
2	7676±136
4	4876±78
5	3849±68
6	2786±63
7	1660±51
8	936±43

Table A.1: Angular distribution at the effective beam energy of 41.67 MeV

A.2 Fusion cross-sections

The total fusion cross-sections at all measured energies for the ^{12}C+^{24}Mg are reported in Table. A.2.

$E_{c.m.}$(MeV)	σ_{fus}(mb)
17.23	450±14
13.89	215±2
13.56	164±3
13.22	135±52
12.89	105±2
12.55	84±1
12.22	80±3
11.88	56±4
11.55	42±2
11.22	30±1
10.88	15.7±0.6
10.55	8.7±0.4
10.21	3.4±0.2
9.88	1.05±0.08
9.71	0.57±0.04
9.54	0.39±0.03
9.38	0.22±0.03
9.21	0.14±0.02
9.04	0.05±0.01
8.88	0.02±0.01
8.54	0.008±0.008

Table A.2: Total fusion cross-sections for the ^{12}C+^{24}Mg system

A.3 Astrophysical S-factor

The astrophysical S-factors for the ^{12}C+^{24}Mg are reported in Table. A.3.

$E_{c.m.}$(MeV)	S(E) (a.u.)
17.23	0.111±0.003
13.89	12.3±0.1
13.56	17.9±0.3
13.22	28.7±0.5
12.89	45.2±0.7
12.55	79±1
12.22	191±7
11.88	283±19
11.55	460±20
11.22	750±30
10.88	916±36
10.55	1244±54
10.21	1238±64
9.88	1020±78
9.71	919±60
9.54	1064±98
9.38	1036±174
9.21	1157±173
9.04	685±183
8.8	417±208
8.54	590±590

Table A.3: S-factor for the ^{12}C+^{24}Mg system

The scaling factor η_o was calculated at the energy value of 11.5 MeV. The value of η_o= 9.43. Hence, $S(E) = E\sigma(E)e^{2\pi(\eta-9.43)}$.

A.4 Logarithmic Slope

The logarithmic slope L(E) for the $^{12}C+^{24}Mg$ calculated using the 'three-point formula' along with the L_{CS} are reported in Table. A.4.

$E_{c.m.}$(MeV)	L_{CS}(MeV^{-1})	L(E) (MeV^{-1})
13.89	1.94	-
13.56	2.01	0.3±0.1
13.22	2.09	0.74±0.01
12.89	2.17	0.71±0.01
12.55	2.26	0.66±0.02
12.22	2.35	0.10±0.03
11.88	2.45	0.45±0.04
11.55	2.56	1.14±0.04
11.22	2.67	1.10±0.05
10.88	2.80	1.65±0.04
10.55	2.93	2.04±0.04
10.21	3.08	2.48±0.04
9.88	3.24	3.38±0.06
9.71	3.32	3.79±0.04
9.54	3.41	3.19±0.04
9.38	3.50	3.05±0.06
9.21	3.59	3.25±0.06
9.04	3.69	4.8±0.1
8.88	3.80	6.7±0.2
8.54	4.02	4.2±0.5

Table A.4: Logarithmic slope for the $^{12}C+^{24}Mg$ system

Bibliography

[1] C. Y. Wong. In: *Physical Review Letters 31,* 12 (1973), pp. 766–769.

[2] S. Landowne C. H. Dasso and A. Winther. In: *Nuclear Physics A 407,* 12 (1993), pp. 221–232.

[3] S. Landowne C. H. Dasso and A. Winther. In: *Nuclear Physics A 405,* 12 (1993), pp. 381–396.

[4] C. L. Jiang et al. In: *Physical review letters 89,* 5 (2002).

[5] L. R. Gasques et al. In: *Phys. Rev. C 76,* 035802 (2007).

[6] G. Montagnoli et al. In: *Physical Review C 97,* 2 (2018), pp. 1–6.

[7] A.T. Kruppa K. Hagino N. Rowley. In: *Computer Physics Communications* 123 (1999), pp. 143–152.

[8] Ö. Akyüz and A. Winther. In: *Proc. Int. School of Physics "Enrico Fermi" Course LXXVII, Varenna* (1979).

[9] R. A. Broglia and A.Winther. *Heavy-Ion Reactions.* Addison-Wesley, New York, 1991.

[10] K. Hagino and N. Takigawa. In: *Prog.Theor.Phys.* 128 (2012).

[11] K. Hagino. *Quantum Many-body Dynamics in low-energy heavy-ion reactions.* University Lecture.

[12] P. Fröbrich and R. Lipperheide. *Theory of Nuclear Reactions.* Clarendon Press, 1996.

[13] B. Borderie and M. F. Rivet. In: *Progress in Nuclear and Particle Physics* 61 (2008), p. 551.

[14] D. L. Hill and J. A. Wheeler. In: *Physical Review 89,* 5 (1953), pp. 1102–1145.

[15] J. R. Leigh et al. In: *Physical Review C 52,* 6 (1995), p. 3151.

[16] M. Beckerman et al. In: *Physical Review Letters 45,* 18 (1980), pp. 1472–1475.

[17] M. Dasgupta et al. In: *Annu. Rev. Nucl. Part. Sci.,* 48 (1998), pp. 401–461.

[18] M. N. Harakeh and A. Van Der Woude. *Giant Resonances*. Oxford University Press, 2001.

[19] N. Takigawa et al. In: *Physics Review C 49,* 5 (1994), p. 2630.

[20] K. Hagino S. Yusa and N. Rowley. In: *Physical Review C 85,* (2012), pp. 1–8.

[21] A. B. Balantekin M. A.Nagarajan and N. Takigawa. In: *Phys. Rev. C 34,* 3 (1986), pp. 894–898.

[22] C.H. Dasso. *Effects of reaction channels in subbarrier fusion reactions (NORDITA–84/11(prepr)). Denmark.*

[23] A. M. Stefanini et al. In: *Physical Review Letters 74,* 6 (1995), pp. 864–867.

[24] H. Esbensen and S. Landowne. In: *Physical Review C 35,* 6 (1987), pp. 2090–2096.

[25] C. L. Jiang et al. In: *Physical Review Letters 93,* 1 (2004).

[26] Giulia Colucci. "A fast ionization chamber for the detection of fusion-evaporation residues produced by the exotic beams of SPES: design, tests and first experiments". PhD thesis. Università degli Studi di Padova, 2018.

[27] T. Ichikawa et al. In: *Physical Review Letters 103,* 20 (2009), pp. 1–4.

[28] T. Ichikawa. In: *Physical Review C 92,* 6 (2015), pp. 1–19.

[29] S. Misicu and H. Esbensen. In: *Physical Review C 75,* 3 (2007), pp. 1–14.

[30] S. Misicu and H. Esbensen. In: *Physical Review C 96,* 11 (2006), pp. 1–4.

[31] E. M. Burbidge et al. In: *Reviews of Modern Physics 29,* 4 (1957), pp. 547–650.

[32] X. Fang et al. In: *Phys. Rev. C 96,* 045804 (2017).

[33] C. L. Jiang et al. In: *Phys. Rev. C 79,* 044601 (2009).

[34] C. L. Jiang et al. In: *Phys. Rev. C 69,* 014604 (2004).

[35] C. L. Jiang et al. In: *Eur. Phys. J. A 54,* 218 (2018).

[36] K. Daneshvar et al. In: *PRC 25,* 1342 (1982).

[37] S. Gary and C. Volant. In: *PRC 25,* 1877 (1982).

[38] G. Montagnoli et al. In: *Nuclear Instrumentations and Methods in Physics Research 547* , 2-3 (2005), pp. 455–463.

[39] D. Shapira et al. In: *Nuclear Instruments and Methods in Physics Research A 551,* 2-3 (2005), pp. 330–338.

[40] G. F. Knoll. *Radiation Detection and Measurement*. John Wiley Sons Inc, IV edition, 2010.

[41] URL: www.srim.org.

[42] URL: http://lise.nscl.msu.edu/pace4.html.

[43] C.L. Jiang et al. In: *Physics review letters 113,* 022701 (2014).

[44] A. Morsad et al. In: *Phys. Rev. C 41,* 988 (1990).

[45] C. L. Jiang et al. In: *Phys. Rev. C 75,* 014613 (2007).